1   **Revision 2**

2   **Substitution of Ti^{3+} and Ti^{4+} in hibonite ($CaAl_{12}O_{19}$)**

3

4   Patricia M. Doyle[1,2,†], Paul F. Schofield[2], Andrew J. Berry[1,2,*], Andrew M. Walker[3‡] and Kevin S.

5   Knight[4,2]

6

7   [1] Department of Earth Science and Engineering, Imperial College London, South Kensington. SW7

8   2AZ. UK

9   [2] Department of Earth Sciences, Natural History Museum, Cromwell Road, London. SW7 5BD. UK

10   [3] School of Earth Sciences, University of Bristol, Wills Memorial Building, Queen's Road, Bristol.

11   BS8 1RJ. UK

12   [4] ISIS Science Division, Rutherford Appleton Laboratory, Chilton, Didcot. OX11 0QX. UK

13

14

15   [†] Present address: Hawai'i Institute of Geophysics and Planetology, University of Hawai'i at

16   Manoa, 96822, USA

17   [*] Present address: Research School of Earth Sciences, Australian National University, Canberra,

18   ACT, 2601 Australia

19   [‡] Present address: School of Earth and Environment, University of Leeds, Leeds, LS2 9JT, UK

20

21

22   **Abstract**

23   The structures of eight synthetic samples of hibonite, with variable Ti oxidation state and Ti

24   concentrations (2.4-15.9 wt% TiO_2) that span the range reported for natural hibonite found in

25   meteorites, were determined by Rietveld refinements of neutron powder diffraction data. Ti^{3+} was

26   found to exclusively occupy the octahedral face-sharing M4 site irrespective of the presence or

27   absence of Ti^{4+}. Ti^{4+} partitions between the trigonal bipyramidal M2 site and the M4 site. The ratio

28   (Ti^{4+} on M2):(Ti^{4+} on M4) appears to be constant for all the samples, with an average of 0.18(2)

29   irrespective of the concentrations of Ti^{3+} and Ti^{4+}. These substitutional sites were shown to be the

30   most stable configurations for Ti in hibonite from calculations using density functional theory,

31   although the predicted preference of Ti^{4+} for M4 over M2 is not as strong as is observed. This is

32   attributed to the different Ti contents of the experimental and calculated structures and suggests that

33   the Ti site occupancies might change between these concentrations. Furthermore, it is shown that

34   Ti has a preference to occupy neighbouring M4 sites such that Ti-Ti interactions occur with

35   stabilization energies of 83 kJ/mol for Ti^{3+}-Ti^{3+} and at least 15 kJ/mol for Ti^{4+}-Ti^{4+}. Features in

36   optical spectroscopy and electron spin resonance data from meteoritic and synthetic hibonites that

1

37   have been used to infer Ti^{3+}/Ti^{4+} are shown to actually derive from these Ti-Ti interactions. The

38   amount of Ti^{4+} in hibonite can be determined from the unit-cell parameters if ΣTi is determined

39   independently. Ti^{3+}/Ti^{4+} in hibonite may record the oxygen fugacity (f_{O2}) of the early solar nebula,

40   however, the existence of Ti^{3+}-Ti^{3+} and Ti^{4+}-Ti^{4+} interactions and the potential for Ti^{4+}-Ti^{3+}

41   interactions need to be considered when interpreting spectroscopic data in terms of Ti valence state

42   and f_{O2}. Hibonite as a single-mineral oxybarometer must be used with caution due to the potential

43   role of crystal chemistry (including Ti-Ti interactions) to stabilise Ti oxidation states independently

44   of f_{O2}.

45

46

47

48   Keywords: hibonite, titanium substitution, site occupancy, CAI, neutron diffraction, density

49   functional theory, oxygen fugacity

2

Introduction

50

51   Some of the oldest materials in the Solar System are the refractory calcium-aluminium-rich

52 inclusions (CAIs) found in undifferentiated chondritic meteorites (Amelin et al. 2002). Hibonite

53 (CaAl$_{12}$O$_{19}$), a mineral found within some CAIs, is thought to be the second major phase to

54 condense from a gas of solar composition (Lodders 2003). Moreover, hibonite is the first mineral

55 to condense that can incorporate significant amounts of polyvalent elements such as Ti, V, Cr and

56 Fe into its structure. As a result, hibonite has the potential to record the conditions present in the

57 early Solar System, in particular the composition and hence oxygen fugacity (f_{O2}) of the nebular

58 gas. For terrestrial materials the intrinsic f_{O2} is usually determined from Fe^{2+}/Fe^{3+}, however, this is

59 impractical for CAIs as the extremely reducing conditions of formation usually result in the

60 presence of metallic Fe (i.e. Fe^0/Fe^{2+}). The most suitable alternative redox sensor is Ti^{3+}/Ti^{4+} (e.g.

61 Grossman et al. 2008) since Ti is a significant component of CAIs and the ratio varies over the

62 range of expected f_{O2}s (Simon et al. 2007). Meteoritic hibonite may contain up to ~ 8 wt% TiO$_2$

63 (Allen et al. 1978) and consequently has the potential to be utilised as a single-mineral

64 oxybarometer.

65

66   Hibonite crystals in CAIs can be colourless, greenish-blue, blue or orange and these

67 differences have been used to infer variations in the oxidation state of Ti, and to a lesser degree V

68 (e.g. Burns and Burns 1984; Ihinger and Stolper 1986); such colour changes have even been

69 reported to occur between the core and rim of individual hibonite crystals (Rout and Bischoff

70 2008). Previous studies of meteoritic hibonite by optical absorption spectroscopy and electron spin

71 resonance (ESR) spectroscopy (Ihinger and Stolper 1986; Beckett et al. 1988) have confirmed the

72 presence of Ti^{3+} and suggested $Ti^{3+}/\Sigma Ti$ (where $\Sigma Ti = Ti^{3+} + Ti^{4+}$) values up to 0.2. However,

73 accurate measurement of Ti^{3+}/Ti^{4+} in materials is not necessarily a simple process. The

74 determination of Ti^{3+}/Ti^{4+} from stoichiometry or wet chemistry is notoriously problematic (e.g.

75 Beckett et al. 1988; Rager et al. 2003), while both optical and ESR spectroscopies are impeded by

76 the presence of Fe, which is ubiquitous in natural systems. Further, the size and inhomogeneity of

77 meteoritic hibonite crystals generally require the use of microbeam techniques. X-ray absorption

78 near edge structure (XANES) spectroscopy and X-ray photo emission electron microscopy

79 (XPEEM) have the potential to non-destructively quantify valence states, including $Ti^{3+}/\Sigma Ti$, with

80 micron (e.g. Berry et al. 2008; Simon et al. 2007) and sub-micron (e.g. Smith et al. 2004; Schofield

81 et al. 2010) spatial resolution, respectively.

82

83   The spectroscopic quantification of $Ti^{3+}/\Sigma Ti$ is strongly dependent on the interpretation of

3

84 spectra from suitable standards. Spectral detail is in turn directly related to the crystal chemistry of

85 the phase in question. Hibonite is crystal chemically complex, having five Al sites onto which Ti

86 may substitute and the preferred site occupancy of Ti is likely to be influenced by its oxidation

87 state. As yet there is no unambiguous description of the structural incorporation of Ti^{3+} and Ti^{4+}

88 into hibonite. We have used neutron powder diffraction (NPD) to structurally characterise a suite of

89 eight synthetic Ti-bearing hibonite samples, where $Ti^{3+}/\Sigma Ti$ varies between 0 and 1. As with X-ray

90 diffraction (XRD), NPD offers excellent contrast between Al and Ti, however, unlike XRD, NPD

91 also provides good contrast between Mg and Al and the fractional coordinates and atomic

92 displacement parameters of the oxygen atoms can be determined with high precision, thereby

93 increasing the certainty of the structural model. The findings of the NPD study are compared to,

94 and supported by, density functional theory (DFT) modelling.

95

96   **Crystal Structure**

97   The structure of hibonite ($CaAl_{12}O_{19}$) was first characterised by Curien et al. (1956) and

98 subsequently refined in a number of XRD studies (Kato and Saalfeld 1968; Utsunomiya et al. 1988;

99 Bermanec et al. 1996; Hofmeister et al. 2004; Nagashima et al. 2010). Hibonite is hexagonal (space

100 group P63/mmc, Z=2, a ~ 5.6 Å and c ~ 22.0 Å; Hofmeister et al. 2004) and exhibits the

101 magnetoplumbite structure-type (Kato and Saalfeld 1968). The hibonite structure (Figure 1) is

102 dominated by polyhedral layers perpendicular to the *c*-axis, in which Ca occupies a 12-coordinated

103 polyhedron, and Al is distributed over five M sites. M1 is a regular octahedron (D_{3d}), M2 is a

104 trigonal bipyramid with an ideal site symmetry of D_{3h}, M3 is a tetrahedron (C_{3v}), M4 is a trigonally

105 distorted octahedron (C_{3v}) and M5 is a strongly distorted octahedron (C_s). The trigonal bipyramidal

106 site is split into two symmetrically-equivalent half-occupied sites above and below the equatorial

107 plane of the bipyramid by the static displacement of the M2 cation from the site-centre (Utsunomiya

108 et al. 1988; Du and Stebbins 2004). Within these pseudotetrahedral M2 sites the cation positions

109 are separated by 0.17-0.27 Å (Bermanec et al. 1996; Hofmeister et al. 2004). The multiplicity of

110 the cation sites and their coordination numbers may be summarised as follows:

111 $^{[12]}Ca^{[6]}M1^{[5]}M2^{[4]}M3_2^{[6]}M4_2^{[6]}M5_6O_{19}$ (where coordination numbers are superscripted in square

112 brackets and the multiplicity of the site is subscripted).

113

114   The arrangement and distribution of the polyhedra in hibonite are such that the structural

115 topology can be considered in terms of a repetition of two distinct polyhedral layers perpendicular

116 to the c-axis (Burns and Burns, 1984; Nagashima et al. 2010). Within one of these layers, referred

117 to as the S-block, the tetrahedral (M3) and octahedral (M1 and M5) polyhedra are arranged as in the

118 spinel structure (Figure 1). These S-blocks are separated by a layer comprising the Ca site, the

4

119   trigonal bipyramidal M2 site and the octahedral M4 site, referred to as the R-block (Kohn and

120   Eckart 1964) or conductor layer (Iyi et al. 1989). The thickness of the R-block (along *z*) equates to

121   the O1-O1 distance between the apical oxygen atoms of the M2 site. The M2 polyhedra are

122   isolated from each other and linked by the M4 and Ca polyhedra. The M4 octahedra share a face,

123   forming isolated face-sharing pairs in which the M4 cations are separated by about 2.59 Å, parallel

124   to *z* (Hofmeister et al. 2004). The hibonite unit cell is formed by stacking R- and S-blocks along *z*

125   according to the sequence RSR'S', where R' and S' are rotated 180º about *z* relative to R and S

126   respectively (Bermanec et al. 1996).

127

128   **Site Substitutions**

129   A range of elements substitute into the hibonite structure (Table 1), with natural hibonites

130   containing Mg^{2+}, Zn^{2+}, Fe^{2+}, Fe^{3+}, Cr^{3+}, V^{3+}, Ti^{3+}, Ti^{4+}, Si^{4+} and Th^{4+} as major elements and the rare

131   earth elements La, Ce and Nd, at levels above 1000 ppm (e.g. Burns and Burns 1984; Beckett et al.

132   1988; Rakotondrazafy et al. 1996). Of particular interest to this study is Ti: Ti^{3+} may substitute

133   directly for Al^{3+}, whereas Ti^{4+} undergoes a coupled substitution with Mg^{2+} for two Al^{3+} (Mg^{2+} +

134   Ti^{4+} ↔ $2Al^{3+}$) in order to maintain charge balance (Allen et al. 1978). Ti^{3+} is thought to occupy the

135   M2 site in hibonite based on crystal field stabilisation theory, and ESR and optical spectroscopies

136   (Burns and Burns, 1984; Beckett et al. 1988). In single crystal XRD studies of terrestrial hibonite,

137   Ti^{4+} has been reported to occupy only the M4 site (Bermanec et al. 1996) and both the M2 and the

138   M4 sites (Nagashima et al. 2010). The site occupancies of various elements in hibonite and

139   structural analogues, including natural and synthetic members of the magnetoplumbite group

140   ($AB_{12}O_{19}$) and β-alumina phases, are summarised in Table 1, indicating a large range of possible

141   sites for Ti^{3+} (M1, M2, M5) and Ti^{4+} (M1, M2, M4, M5).

142

143   **Experimental**

144   Synthesis

145   A suite of eight Ti-bearing hibonite samples was synthesized, two Ti^{3+} end-member samples

146   with $Ti^{3+}/\Sigma Ti = 1$, two Ti^{4+} end-member samples with $Ti^{4+}/\Sigma Ti = 1$ and four mixed-valent samples

147   with $Ti^{3+}/\Sigma Ti$ between 0 and 1. All samples were synthesised at ~1400 ºC, which is within the

148   stability field of hibonite in a gas of nebular composition (Yoneda and Grossman 1995) and well

149   below the experimentally determined incongruent melting temperature (1850 ± 10 ºC in the CaO-

150   MgO-Al_2O_3 ± SiO_2 system; De Aza et al. 2000; Vázquez et al. 2003).

151

152   Stoichiometric mixtures of pre-dried $CaCO_3$, Al_2O_3, TiO_2 and MgO were pressed into pellets

153   and heated at ~1400 ºC for ~30 h in graphite and an atmosphere of CO ($\log f_{O_2} = -16$) for the Ti^{3+}

5

154   end-member and mixed-valent samples and in Pt and CO_2 (logf_{O_2} = -3) for the Ti^{4+} end-member

155   samples. The synthesis of the mixed-valent samples relied on stoichiometry to control $Ti^{3+}/\Sigma Ti$

156   (noting the coupled substitution of Ti^{4+} and Mg^{2+}) at constant fO$_2$. All samples were cooled from

157   1400 to 600 ºC over ~2 h. The Ti^{3+} end-member samples were essentially single phase after a

158   single sinter whereas the yield of Ti^{4+} hibonites was improved by a second sinter. At least 5 g of

159   each sample was prepared by combining the products of multiple individual experiments that were

160   sufficiently similar based upon XRD (Schofield et al. 2002). The chemical formulae of these Ti-

161   bearing hibonites and identities of any secondary phases identified are given in Table 2. The Ti^{3+}

162   end-member and mixed-valent samples were all blue whereas the Ti^{4+} end-member samples were

163   white.

164

165   Throughout this manuscript the samples are identified by reference to their Ti per formula

166   unit (pfu) and $Ti^{3+}/\Sigma Ti$ ratios in the form (Ti pfu, $Ti^{3+}/\Sigma Ti$). For example, the sample (0.5,1.0) will

167   have 0.5 Ti pfu and all the Ti will be Ti^{3+} giving a chemical formula of $CaAl_{11.5}Ti_{0.5}O_{19}$. The

168   sample (1.0,0) will have 1.0 Ti^{4+} pfu (and 1.0 Mg^{2+} pfu) giving a chemical formula of

169     $CaAl_{10.0}Ti_{1.0}Mg_{1.0}O_{19}$.

170

171   Scanning electron microscopy

172   Sintered samples were mounted in epoxy resin and the composition determined by energy

173   dispersive spectrometry using a Jeol 5900LV EDS SEM operated at 10 kV and 2 nA. The

174   fluorescence was calibrated to the K-lines of Ca in $CaSiO_3$, Al in Al_2O_3, Ti in TiO_2 rutile and Mg

175   and Si in $Mg_{1.6}Fe_{0.4}SiO_4$. Matrix corrections were made using the XPP routine (Oxford

176   Instruments).

177

178   Neutron powder diffraction

179   Neutron time-of-flight powder diffraction data were collected on the fixed geometry, high

180   resolution diffractometer HRPD (Ibberson et al. 1992) at the ISIS neutron spallation source,

181   Rutherford Appleton Laboratory, U.K. Between 2.8 and 4.4 g of sample were packed into an In

182   sealed cylindrical V can with an external diameter of 11 mm, and loaded into the sample tank,

183   which was pumped down to a vacuum below 10^{-4} Torr. Diffraction patterns were collected for

184   exposure times between 100 and 152 µAhours with ISIS operating at 40 Hz, an average proton

185   current of ~160 µA and upstream neutron choppers selecting one pulse in five.

186

187   Data were collected simultaneously in both the high-resolution backscattering and 90º

188   detector banks in the time-of-flight ranges 32000 µs to 126000 µs and 32000 µs to 130000 µs

6

189   respectively. Diffraction spectra were focused, binned as $\Delta t/t$ = 0.0005 and 0.0003 for the 2θ = 90 º

190   and backscattering data respectively, background subtracted, normalised to the incident flux

191   distribution using the isotropic incoherent scattering from a V rod and finally corrected for

192   absorption and self-scattering. The resulting data were subsequently formatted for use in a two-

193   bank whole profile Rietveld refinement.

194

195   Structural refinement

196   Structural parameters were determined from whole pattern profile fitting of the diffraction

197   data within the GSAS (General Structure Analysis System) code of Larson and Von Dreele (1994)

198   interfaced with EXPGUI (Toby 2001). The first refinement for each sample was based upon the

199   structural model of Hofmeister et al. (2004) using coherent scattering lengths from Sears (1992) of

200   4.70 fm (Ca), 3.449 fm (Al), -3.438 fm (Ti), 5.38 fm (Mg) and 5.803 fm (O). Peak profiles were

201   modelled using the model-dependent Le Bail method with three sample-dependent variables and

202   backgrounds were modelled using a five-term shifted Chebyschev function. Thereafter, the structure

203   was refined using the Rietveld method (Rietveld 1969; 2000). The profiles from the two data banks

204   were scaled, the structural parameters of additional phases (if any) added and scaled relative to

205   hibonite, and then refined simultaneously. The unit-cell parameters for hibonite were refined first,

206   followed by the atomic coordinates and atomic displacement parameters (ADP).

207

208   Mg and Ti were initially included in the refinements based upon the stoichiometry calculated

209   by EDS and then varied as required by the refinement process. Ti site occupancies for the two Ti^{3+}

210   end-member samples (0.20,1.0) and (0.33,1.0) were allowed to vary within the least squares

211   refinements. For the Ti^{4+} end-member and the mixed-valent samples, however, the Mg and Ti site

212   occupancies were fixed during the least squares refinements and manually iterated between

213   refinement cycles. Attempts at discriminating between the fractional coordinates and ADPs of

214   different atoms on the same site were unsuccessful, and consequently the fractional coordinates and

215   ADPs for all atoms on a specific site were constrained to be identical. The proportions of Ti (or Mg)

216   and Al on a site were constrained to sum to 1, except for the M2 site where the cation is axially

217   displaced from the mirror plane and thus the maximum occupancy is 0.5.

218

219   Density functional theory modelling

220   DFT (Hohenberg and Kohn 1964; Kohn and Sham 1965) based calculations within the

221   generalised gradient approximation (GGA) were used to determine the energy and structure of a

222   range of Ti substitutions in hibonite. Along with pure $CaAl_{12}O_{19}$ hibonite, simulations of various

223   notionally isolated point defects were performed. Specifically, we considered the direct substitution

7

224   of Al by Ti^{3+}, the substitution of Al by Ti^{4+} coupled to a charge balancing substitution of Mg for Al,

225   and cases where small clusters of Ti defects form. The GGA functional of Perdew et al. (1996) was

226   used to describe exchange and correlation, and our calculations made use of the SIESTA

227   methodology and code (Soler et al. 2002), which takes advantage of a strictly localised atom-like

228   basis set and pseudopotentials to achieve good computational performance for large systems.

229

230   The basis sets and pseudopotentials for Ti, Mg, and O in the calculations were taken from

231   previous work on Ti incorporation in olivine (Berry et al. 2007; Walker et al. 2007), zircon (Tailby

232   et al. 2011), and the thermodynamics of qandilite (Palin et al. 2008), which encompass a wide range

233   of cation coordination environments. For Al we made use of the pseudopotential and basis set

234   derived for a study of the structure of γ-alumina (Paglia et al. 2005), while for Ca we used a basis

235   set optimised for the study of perovskite using the method of Junquera et al. (2001) with double

236   zeta polarised valance states (4s and 4p), single zeta polarised semi-core states (3s and 3p) and

237   added 3d states. The Ca pseudopotential was refitted from the version derived by Junquera et al.

238   (2001), which made use of the local density approximation, to GGA all-electron results using a

239   small partial core correction to avoid an undesirable kink in the fitted potential.

240

241   SIESTA makes use of a real space grid as an auxiliary basis for the calculation of the

242   exchange-correlation and Hartree energies. A kinetic energy cut-off of 250 Ry with $2 \times 2 \times 2$ grid

243   cell sampling was found to give sufficiently accurate results and minimise rippling artefacts. The

244   structure and energy of pure hibonite was derived from variable cell parameter calculations on a

245   single (64 atom) unit-cell. This calculation made use of a $5 \times 5 \times 2$ Monkhorst–Pack mesh in

246   reciprocal space. Calculations containing defects were all performed in a 256 atom supercell where

247   the lattice vectors were doubled in the *x* and *y* directions to give a minimum separation of 11.2 Å

248   between periodic images of any atom within the structural layers and a 22.0 Å separation along *z*.

249   These defect calculations only sampled reciprocal space at the Γ-point and the cell parameters were

250   not permitted to vary from those calculated for the perfect system (the defect calculations were thus

251   designed to simulate isolated point defects). Geometry optimisation was performed using the

252   Broyden and conjugate gradients algorithms with stop parameters of a maximum force of 0.01

253   eV/Å on any atom and (where the cell parameters were allowed to vary) a maximum stress of 200

254   bar on any component of the stress tensor.

255

256   **Results**

257   The eight samples studied by NPD encompass the full range of Ti^{3+}, Ti^{4+}, and ΣTi contents,

258   and Ti^{3+}/ΣTi that have been measured in meteoritic hibonite (Figure 2) as well as more Ti^{3+}-rich

8

259   and Ti^{4+}-rich compositions.

260

261   Rietveld analysis

262   The results of the Rietveld refinement of the NPD data for all eight synthetic Ti-bearing

263   hibonite samples are given in Table 3 (lattice parameters and site occupancies) and Table 4 (atomic

264   coordinates, displacement parameters). The whole-profile Rietveld powder statistics (as defined by

265   Young, 1993) for the simultaneous refinement of the 90º and backscatter detector-bank datasets

266   were $_wR_p$ = 2.3 - 3.4 % and R_p = 2.5 - 4.6 %. The observed, calculated and difference profiles for

267   the Ti^{3+} end-member sample (0.20,1.0) and the Ti^{4+} end-member sample (0.98,0) are shown in

268   Figure 3. Initially the Ti and Mg pfu were set to those determined by EDS but were allowed to vary

269   during the refinements. It seems reasonable to expect a 1:1 correlation between the Rietveld refined

270   and EDS determined Ti and Mg contents, and this was observed (Figure 4). In this work the refined

271   structural data are plotted against Mg and Ti pfu values from the Rietveld refinements.

272

273   Most of the Ti^{4+}-bearing samples have a degree of compositional variability, as evident from

274   the large uncertainties of the Al_2O_3 and TiO_2 values (relative to those of the Ti^{3+} end-members) in

275   Table 2, which resulted in asymmetric peak broadening of their diffraction data. Two strategies

276   were applied to account for this peak asymmetry. Firstly, the variability in the Ti-content was

277   considered by incorporating a Ti-poor hibonite into the Rietveld model as a minor secondary phase.

278   Secondly, the refinements were performed assuming a homogeneous sample and accepting slightly

279   increased residuals and fit statistics. Both refinement strategies produced the same structural model

280   and Ti and Mg site-occupancies. The data presented in Tables 3 and 4, and discussed throughout

281   are those obtained using the second of these strategies.

282

283   Throughout the Rietveld analyses the ADPs were constrained to be isotropic. Single-crystal

284   XRD studies of $CaAl_{12}O_{19}$ have shown, however, that the ADP for the M2 cation is relatively

285   anisotropic with U_{33} (parallel to z) four times larger than U_{11} and U_{22} (Hofmeister et al. 2004;

286   Utsunomiya et al. 1988). The degree of anisotropy determined for the M2 ADP in natural hibonite

287   that may contain additional cations, such as Ti, on the M2 site was found to be even larger

288   (Hofmeister et al. 2004; Nagashima et al. 2010). This anisotropy of the displacement parameter for

289   M2 relates to a combination of axial off-centring of the cation from the equatorial plane and

290   anisotropic thermal motion, although the static rather than dynamic contributions are likely to be

291   dominant (Nagashima et al. 2010). The ADP for the M2 cation in our refined models (U_{iso} in Table

292   4) is ~1.5 - 2 times larger than the average ADP for the cations on the four other M sites, consistent

293   with previous results (Bermanec et al. 1996; Hofmeister et al. 2004; Nagashima et al. 2010). In an

9

294   attempt to quantify the anisotropy of the M2 ADP, additional refinements were performed in which

295   the ADP for this site could vary anisotropically. While the results should be treated cautiously due

296   to the high degree of freedom in the refinement, it was found that the ADPs for M2 were distinctly

297   anisotropic with U_{33} being approximately double U_{11} and U_{22}.

298

299   DFT modelling

300   To provide a reference structure for the defect calculations, and as a test of the accuracy of the

301   methodology, SIESTA was first used to calculate the atomic positions and lattice parameters of

302    $CaAl_{12}O_{19}$ hibonite. The initial structure was based on the hibonite refinement reported by

303   Bermanec et al. (1996) with the impurities removed. The 5-coordinate M2 site deserves special

304   comment. In the P63/mmc space group the three equatorial oxygen sites of this trigonal bipyramid

305   lie on a mirror plane but in hibonite the central M2 atom is displaced and, when averaged over a

306   large sample, the atomic occupancy is split evenly over two 4e sites. As a result, in any given

307   trigonal bipyramid the M2 Al atom is displaced ~0.3 Å in either the positive or negative z direction

308   and one of the 4e sites in the bipyramid is occupied and the other unoccupied. This locally breaks

309   the crystal symmetry (removing the mirror plane) and the partial occupancy reveals dynamic and

310   static averaging in the diffraction experiment. The SIESTA calculation describes an infinite array

311   of copies of a single unit-cell without this averaging. As there are two M2 sites in the unit-cell

312   there are two possible structures: one with the M2 Al atoms displaced in the same z direction (~11.1

313   Å M2-M2 spacing along c) and one where they are displaced in opposite directions (alternating

314   ~10.9 and ~11.4 Å spacing along z). Both starting structures were investigated and it was found

315   that while the distortion was preserved in the DFT calculations (i.e. the Al atom did not move to the

316   mirror plane) the structures had equal energies. This is consistent with the presence of disorder on

317   this site as indicated by the ADPs and partial site occupancies. Having generated the starting

318   hibonite structures, energy minimisation was undertaken in which the lattice parameters and atomic

319   positions were allowed to vary with no symmetry imposed. This process yielded lattice parameters

320   of a = b = 5.61 Å, c = 22.05 Å, $\alpha = \beta = 90.0°$, and $\gamma = 120.0°$. The larger lattice parameters (by

321   ~1%) compared to the experimental determination of Hofmeister et al. (2004) are expected for DFT

322   calculations utilising a GGA functional.

323
324   The structure of the optimised cell was used to build the 256 atom supercell for defect

325   calculations. Six sets of defect calculations were performed. (1) An Al atom on each of the five M

326   sites was replaced in turn by a Ti atom leading to the isovalent substitution of Al^{3+} by Ti^{3+}. (2)

327   Each of these calculations was repeated with one less electron in the simulation cell giving a

328   positively charged system and describing the substitution of Al^{3+} by Ti^{4+}. (3) Each of the isovalent

10

329   calculations was also repeated with the Ti atom being replaced by a Mg^{2+} giving a negatively

330   charged system with Mg^{2+} substituting for Al^{3+}. (4) One Al atom was replaced by Ti and one by

331   Mg leading to the charge-neutral coupled substitution of two Al^{3+} for a Ti^{4+} and Mg^{2+}. For each M

332   site occupied by Al there are several inequivalent ways of introducing the Mg to make a coupled

333   substitution. Every case where the Ti and Mg polyhedra share a face, edge or vertex (21 distinct

334   coupled defects) was investigated and, guided by the results of the calculations on isolated Ti^{4+} and

335   Mg^{2+} substitutions, three cases where the Mg is on a M3 site with the Ti on a nearby M2 or M4 site

336   (M3 does not share a vertex with M2 or M4) were also considered. (5) Two Ti atoms were placed

337   on adjacent Al sites to give neutral two-atom defect clusters (nominally of Ti^{3+} ions). (6) Two Ti

338   and two Mg atoms were added to form neutral four-atom clusters (nominally containing Ti^{4+} ions).

339   In cases (5) and (6), only a small subset of the vast number of possible atomic configurations were

340   considered with the choice based on the earlier calculations, the generation of simple structures and

341   the NPD results. Each defect configuration was subjected to geometry optimisation that allowed all

342   atomic positions (but not the lattice parameters) to vary in order to evaluate the defect stability.

343   Energies are given in Tables 5 and 6 where the defect structures are described using Kröger-Vink

344   notation.

345
346   *Isolated defects*
347

348   If Ti substitutes as isolated trivalent ions it will dominantly occupy the 5-coordinate M2 site

349   as this incorporation mechanism has the lowest energy (Table 5). The energies of the charged cells

350   containing isolated Mg^{2+} and Ti^{4+} ions suggest that, if the necessary charge balancing defect can be

351   assumed to not alter the structure or energy of the defect site, Mg^{2+} will occupy the M3 site and Ti^{4+}

352   will occupy the M2 site.

353
354   As well as energies, the SIESTA calculations also yield the detailed structure of each defect.

355   Considering isolated defects, the Ti atom in the Ti_{Al2}^{x} defect is located close to the ideal mirror

356   plane and, unlike Al on the M2 site, is not significantly displaced along *z*. There are thus two Ti-O1

357   bonds of approximately the same length (2.231 and 2.237 Å), which are between the short (2.062

358   Å) and long (2.357 Å) bond lengths calculated for Al on this site. However, the threefold rotation

359   axis normal to the equatorial plane of the M2 trigonal bipyramid is broken when Ti^{3+} is present on

360   the site. Instead of three 1.769 Å Al-O3 bonds the three Ti-O3 bonds are 1.903, 1.916 and 1.841 Å.

361   The average Ti-O bond length is thus slightly longer than the average Al-O bond length, both

362   calculated using DFT (2.03 Å versus 1.95 Å). In contrast, the Ti^{4+} defect on the M2 site does not

363   break this 3-fold rotational symmetry. Ti^{4+} is also located close to the mirror plane with the two Ti-

11

364   O1 bonds having lengths of 2.169 and 2.175 Å. The three Ti-O3 bonds are 1.806 Å, resulting in an

365   average Ti^{4+}-O bond length of 1.95 Å, which is equal to the Al-O bond length for this site.

366

367   *Ti-Mg interactions*

368   Coulombic interactions will penalise the formation of the isolated Ti^{4+} and Mg^{2+} defects

369   considered above and while these may tend to be entropically stabilised, especially at high

370   temperatures and low impurity concentrations, the formation of charge-neutral defect clusters is

371   perhaps more realistic for the samples synthesized in this study. In order to consider this

372   possibility, charge-neutral simulation super-cells were constructed containing both Ti and Mg on M

373   sites that are close together. The energies of these simulation cells after geometry optimisation are

374   reported in Table 6. These data show that the most stable configuration for a Ti^{4+} defect charge-

375   balanced by a Mg^{2+} defect is for Mg^{2+} to occupy an M3 site and Ti^{4+} to occupy either an M2 or M4

376   site, with the M2 site being the lower energy configuration. Importantly, the energy does not

377   correlate with the Ti^{4+} - Mg^{2+} separation; indeed the Ti^{4+} and Mg^{2+} polyhedra do not share vertices

378   in the lowest energy configurations. These configurations have Ti^{4+} and Mg^{2+} on the M sites that

379   are the lowest energy incorporation mechanisms for the isolated impurities. This indicates that the

380   locations of Ti^{4+} and Mg^{2+} in the charge-neutral defect cluster are controlled by the elemental site

381   preference, and not by short-range interactions between the defects. The energies reported in Tables

382   5 and 6 can be used to determine if these cluster defects are favorable relative to the isolated defects

383   by evaluating the binding energy, which is the energy change of the reaction:

384         $$CaAl_{10}Ti^{4+}Mg^{2+}O_{19} + CaAl_{12}O_{19} \rightarrow CaAl_{11}Ti^{4+}O_{19} + CaAl_{11}Mg^{2+}O_{19}$$
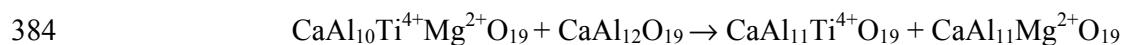
385   or, using Kröger-Vink notation to specify the defect sites:

386         $$\{Ti_{Al(2)}^{\bullet} Mg_{Al(3)}{}'\}_{(b)} \rightarrow Ti_{Al(2)}^{\bullet} + Mg_{Al(3)}{}'.$$
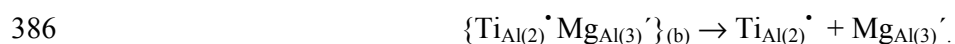
387   When evaluating the energy of this reaction it is important to account for the Coulombic interaction

388   between charged defects in the periodic replicas of the supercells on the right-hand side. This

389   contribution to the energy only varies slowly with supercell size and the important leading term can

390   be removed using the approach described for cubic systems by Leslie and Gillan (1985) and, for the

391   general case, by Woodley et al. (2003). The approach is to approximate the interaction as the energy

392   of an infinite periodic array of point charges, with the same geometry and charge as the point

393   defects, embedded in a dielectric continuum and to subtract this energy from the energy of the

394   defect-bearing supercells. Unfortunately, we do not know the static relative permittivity of hibonite

395   but we can place bounds on the magnitude of the binding energy between the Ti^{4+} and Mg^{2+} point

396   defects. An upper bound of 1.92 eV (~124 kJ/mol Ti) is obtained by neglecting the correction term

397   and a lower bound of 0.49 eV (~47 kJ/mol Ti) results from the minimum shielding that is likely to

398   be provided by the hibonite crystal (i.e. assuming a reasonable lower bound on the relative

399   permittivity of 3.0 and applying this to the full correction from the energy of a periodic array of ions

12

400   with unit charge in a vacuum, which is -1.1797 eV per charged supercell). Even for the lower bound

401   the formation of $\{Ti_{Al(2)}{}^{\bullet}Mg_{Al(3)}{}'\}_{(b)}$ is of lower energy than the isolated $Ti_{Al(2)}{}^{\bullet}$ and $Mg_{Al(3)}{}'$ defects

402   and thus bound defects are expected to dominate.

403

404   *Ti-Ti interactions*

405   The concentration of Ti in the samples with high Ti contents is such that the defects must, on

406   purely geometrical grounds, be close together and thus interact. Calculations were performed to

407   investigate, for both Ti^{3+} and Ti^{4+}, if Ti-Ti interactions alter the structure or energetics of the defects

408   and if the interactions provide a driving force for Ti clustering. Based on the energies of the

409   isolated Ti^{3+} defects and the results of the NPD study, a likely configuration for stabilising pairs of

410   bound Ti^{3+} impurities is for these ions to occupy adjacent M4 sites, as these are low-energy isolated

411   defect sites that share faces in the structure. The energy and structure of this $\{Ti_{Al(4)}{}^{x}Ti_{Al(4)}{}^{x}\}$ defect

412   was calculated and the nature of the Ti – Ti interaction found by considering the energy of the

413   reaction:

414                         $2\ CaAl_{11}TiO_{19} \rightarrow CaAl_{10}Ti_2O_{19} + CaAl_{12}O_{19}$

415   where the left hand side represents the lowest energy isolated Ti^{3+} impurities and the right hand side

416   the coupled defect structure. In Kröger-Vink notation this reaction can be written as:

417                         $2\ Al_{Al(4)}{}^{x} + 2\ Ti_{Al(2)}{}^{x} \rightarrow \{Ti_{Al(4)}{}^{x}Ti_{Al(4)}{}^{x}\} + 2\ Al_{Al(2)}{}^{x}$
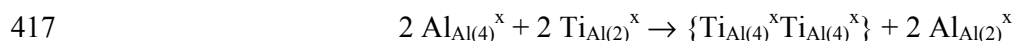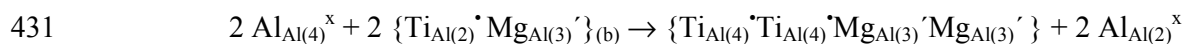
418   Using the data in Tables 5 and 6, the energy change of this reaction is -1.72 eV (83 kJ/mol of Ti)

419   and Ti^{3+} impurities are thus expected to occupy adjacent face-sharing M4 octahedra.

420

421   Similar calculations were performed to investigate the possibility of clustering of Ti^{4+}

422   impurities. An added complication in this case is the need for charge balancing Mg^{2+} defects, which

423   on the basis of the energies of the various isolated defects and the NPD results are found on the M3

424   site. The simplest starting configuration for such a two-Ti^{4+}, two-Mg^{2+} defect cluster is to place one

425   Mg^{2+} in the spinel layer above two Ti^{4+} defects on M4 sites and one Mg^{2+} in the spinel layer below

426   the Ti^{4+} defects. The four defects in the cluster thus form a line parallel to z and have no net dipole.

427   The stability of this $\{Ti_{Al(4)}{}^{\bullet}Ti_{Al(4)}{}^{\bullet}Mg_{Al(3)}{}'Mg_{Al(3)}{}'\}$ configuration is found by considering the

428   energy of the reaction:

429                         $2\ CaAl_{10}MgTiO_{19} \rightarrow CaAl_8Mg_2Ti_2O_{19} + CaAl_{12}O_{19}$

430   or, in Kröger-Vink notation:

431               $2\ Al_{Al(4)}{}^{x} + 2\ \{Ti_{Al(2)}{}^{\bullet}Mg_{Al(3)}{}'\}_{(b)} \rightarrow \{Ti_{Al(4)}{}^{\bullet}Ti_{Al(4)}{}^{\bullet}Mg_{Al(3)}{}'Mg_{Al(3)}{}'\} + 2\ Al_{Al(2)}{}^{x}$

432   which is -0.32 eV (15 kJ/mol of Ti). This low binding energy suggests that Ti^{4+} defect clustering

433   will be limited to high Ti contents and low temperatures. This is consistent with the NPD results

13

434   for samples with high Ti contents, which show that Ti^{4+} preferentially occupies the M4 site, and

435   indicates that Ti site occupancies might change with Ti concentration.

436   The computational results are all for defects at zero Kelvin in the dilute limit. The potential

437   effects of higher temperatures and defect concentrations arise from configurational entropy, which

438   may allow non-ground state defect sites to become occupied. For the single isolated defects this

439   effect can be relatively easily explored using elementary Boltzmann statistics, knowledge of the

440   energy difference between the defect sites, and the site multiplicities. For Mg^{2+} the large (0.83 eV;

441   ~80 kJ/mol of Mg) energy difference between substitution at M3 and the other sites means that

442   essentially all Mg^{2+} is expected to be found on this site at all realistic temperatures. For the single

443   isolated Ti^{3+} and Ti^{4+} defects, where the difference in energy between different sites is lower, we

444   only find significant occupancies (>20%) of sites other than M2 above 1500 K. For the defect

445   clusters only a small subset of the enormous number of possible Ti^{3+}, Ti^{4+} and Mg defect cluster

446   configurations have been considered and this makes quantification of the site occupancies as a

447   function of temperature and Ti content impossible. One approach, which is beyond the scope of the

448   current study, would be to use DFT calculations to parameterize an effective Hamiltonian for cation

449   interactions that is subsequently used as input to Monte Carlo simulations of defect clustering and

450   site occupancy as a function of temperature (e.g. Warren et al. 2001, Palin et al. 2008). However,

451   even without such a study we can make qualitative predictions of the likely effects. Increasing

452   temperature will always make the entropic contribution more important and tend to break up defect

453   clusters and allow multiple different defect configurations to co-exist. Increasing the Ti content will

454   have the opposite effect and tend to result in more clustering of defects; but these effects cannot be

455   quantified without explicit calculations involving all possible defect configurations. One problem

456   that would significantly complicate such a study is the possibility of interactions between Ti^{3+} and

457   Ti^{4+} defects, as the self-interaction problem in DFT will lead to excessive electron delocalization

458   and equalization of the charge on the two defects (e.g. Cramer and Truhlar 2009).

459

460   **Discussion**

461   Site occupancy analysis

462   The site occupancies determined from the refinements of the NPD data are unambiguous and

463   define the substitution mechanisms of Ti^{3+} and Ti^{4+} into these hibonite samples (Table 3). There

464   were no prior assumptions regarding which sites Ti^{3+}, Ti^{4+} and Mg^{2+} would occupy and refinements

465   were attempted with these cations occupying each M site in turn. All models in which Ti and Mg

466   were placed on any site other than those in Table 3 resulted in rapidly diverging refinements or

467   strongly non-physical structural parameters. For the Ti^{3+} end-member samples, (0.20,1.0) and

468   (0.33,1.0), Ti only occupies the face-sharing M4 octahedral site. For the Ti^{4+} end-member samples,

14

469   (0.44,0) and (0.98,0), Ti occupies both the M4 and trigonal bipyramidal M2 sites, while Mg^{2+} only

470   occupies the tetrahedral M3 site. In the mixed-valent samples Ti occupies the M2 and M4 sites and

471   Mg^{2+} is again exclusively located on M3. The refinements do not explicitly distinguish Ti^{3+} from

472   Ti^{4+}, however, there is no reason to expect that the substitution mechanisms identified for Ti^{3+} and

473   Ti^{4+} cannot be applied to the mixed-valent samples. Accordingly, within the mixed-valent hibonites

474   we suggest that Ti^{3+} only occupies M4 and Ti^{4+} occupies both the M2 and M4 sites.

475

476   For the samples in this study it is reasonable to expect that Ti^{4+} undergoes a coupled

477   substitution with Mg^{2+} to maintain charge balance within the structure and that Ti^{4+} pfu = Mg^{2+} pfu.

478   Given that Ti^{3+} only occupies M4 while all the Ti on M2 is Ti^{4+}, the proportions of Ti^{3+} and Ti^{4+} on

479   M4 can then be calculated (Table 3). The Ti^{4+} occupancies of M2 and M4 increase linearly as a

480   function of Ti^{4+} content irrespective of whether the samples are Ti^{4+} end-members or mixed-valent

481   (Figure 5a,b). Furthermore, the partitioning of Ti^{4+} between the M2 and M4 sites appears to be

482   consistent across the entire suite of samples (Table 3), with an average of 0.18 ± 0.02, irrespective

483   of the concentration of Ti and the Ti^{3+}/Ti^{4+} ratio. The DFT site predictions for Ti^{4+} also indicate a

484   preference for M4 over M2, although the predicted preference is not as strong as that observed by

485   NPD. This difference may be attributed to the different Ti contents in each case, suggesting that

486   Ti^{4+} site occupancy could be influenced by concentration. In studies of terrestrial hibonite using

487   single crystal XRD Ti^{4+} has been reported to occupy both the M2 and M4 sites (Nagashima et al.

488   2010) but also only the M4 site (Bermanec et al. 1996). The ratio of the partitioning of Ti^{4+}

489   between M2 and M4 reported by Nagashima et al. (2010) is 0.39, which is double the average value

490   of that found here. These discrepancies can be attributed to the refined occupancies of Ti^{4+} on M2.

491   The refined structure of Nagashima et al. (2010) has 0.62 Ti pfu, compared to the chemical formula

492   of the hibonite crystal which has with 0.52 Ti pfu. Additionally, the crystal contained up to 0.04

493   pfu of Fe, which was not included in the refinement. As Fe is a stronger scatterer of X-rays than Ti,

494   the modelling of a significant amount of Fe by Ti on a single site is likely to cause an artificially

495   increased Ti occupancy in order to compensate for the reduced scattering from that site in the

496   structural model. The crystal of Bermanec et al. (1996) contained 0.3 Fe pfu, which was found to

497   occupy the M2 site. Given that the proportion of Fe on M2 is an order of magnitude greater than

498   that expected for Ti, the Fe would mask the presence of Ti. It is also possible that the large

499   proportion of Fe on M2 precluded the substitution of Ti onto this site (Kreber and Gonser 1976).

500

501   The refinements of the NPD data clearly show that all Mg^{2+} occupies the tetrahedral M3 site.

502   This is supported by DFT calculations (Table 5), which indicate that this is the most stable site for

503   Mg^{2+} by 0.83 eV (~80 kJ/mol of Mg). In previous studies of hibonite and structurally similar

15

504 compounds (Table 1; Abrahams et al. 1987) Mg could only be inferred to occupy the tetrahedral

505 site due to the difficulty of distinguishing between Mg and Al by XRD.

506

507   Optical absorption spectra of both natural and synthetic Ti- and Mg-bearing blue hibonite

508 exhibit a strong absorption band at 715 nm, the intensity of which has been used to infer f_{O2}

509 (Ihinger and Stolper 1986). It was argued that Ti^{3+} did not occupy an octahedral site because this

510 absorption band differed in energy from that of Ti^{3+} in octahedral coordination in Al_2O_3 . Instead

511 Ti^{3+} was thought to occupy the five-coordinate M2 site (Burns and Burns 1984). The absorption

512 spectra of Ti^{3+}- and Ti^{4+}-bearing Al_2O_3, however, exhibit a strong band near 750 nm assigned to

513 Ti^{3+}-Ti^{4+} interactions (Sanchez et al. 1988; Aggarwal et al. 1988; Yamaga et al. 1994). Similar

514 interactions could produce the 715 nm absorption band in hibonite given that both Ti^{3+} and Ti^{4+}

515 occupy the M4 site and that neighbouring M4 octahedra form isolated face-sharing pairs.

516

517   The orientation dependence of ESR spectra recorded for a single crystal of meteoritic hibonite

518 found that the maximum g-tensor was parallel to the c-axis (Beckett et al. 1988). These spectra are

519 similar to those of Ti^{3+}-doped β-alumina, in which Ti^{3+} occurs in rhombically distorted octahedral

520 coordination and the orientation of the g-tensor maximum does not correspond to the direction of

521 maximum site distortion as expected, but is collinear with the Al-Al direction (Barret et al. 1985).

522 That is, the orientation of the g-tensor maximum is consistent with the presence of a next nearest

523 neighbour Ti, as expected for Ti occurring as clustered pairs (Yamaga et al. 1994). M4 in hibonite

524 is a rhombically distorted octahedral site and forms face sharing pairs such that the short M4-M4

525 cation direction is parallel to the crystallographic c-axis. As a result, the ESR data of Beckett et al.

526 (1988) can be re-interpreted as indicating that Ti^{3+} occupies the M4 site with the g-tensor maximum

527 corresponding to the Ti-Ti interaction parallel to the c-axis, and thus is in agreement with the NPD

528 model.

529

530   NPD shows that Ti^{3+} occupies the M4 site in hibonite, and furthermore, our DFT calculations

531 and optical absorption and ESR spectra in the literature are consistent with Ti^{3+} occupying M4 such

532 that Ti-Ti interactions occur across the shared face of the $M4_2O_9$ pairs. Indeed, the DFT

533 calculations show a stabilization energy of ~ 83 kJ/mol for such Ti^{3+}-Ti^{3+} interactions. DFT also

534 suggests that a clustering model involving Ti^{4+} on M4 sites is favourable relative to isolated Ti^{4+}

535 defects. What is not clear, however, is whether Ti^{3+}-Ti^{3+} and/or Ti^{4+}-Ti^{4+} interactions are favoured

536 over Ti^{3+}-Ti^{4+} interactions, an issue that is beyond the scope of the DFT calculations performed and

537 difficult to resolve with NPD. Nevertheless it is an important issue, for while the characteristic blue

538 colour of many meteoritic hibonites is related to the presence of Ti^{3+}, the intensity of this colour

16

539   will not be a good indicator of the concentration of Ti^{3+}, or the Ti^{3+}/Ti^{4+} ratio, if Ti^{3+} is involved in

540   more than one type of Ti-Ti interaction. Moreover, the strong feature at 715 nm present in optical

541   absorption spectra is not simply related to the amount of Ti^{3+}, but to the number of Ti^{3+}-Ti^{4+}

542   interactions, which may not equate to the amount of Ti^{3+}.

543

544   Structural modifications

545   The larger sizes of Ti^{3+} and Ti^{4+} relative to Al^{3+} (Shannon 1976) suggest that the

546   incorporation of Ti will cause an expansion of the unit cell. Indeed, the increase in the refined unit

547   cell parameters as a function of Ti is essentially linear (Table 3, Figure 6a,b). The increase in the

548   size of the unit cell as a function of Ti pfu is not isotropic and the c/a ratio decreases linearly with

549   increasing Ti (Figure 6c). Also shown in Figure 6 are the unit cell parameters of synthetic

550    $CaAl_{12}O_{19}$ (Hofmeister et al. 2004), synthetic Ti^{3+}-bearing $CaAl_{10.1}Ti_{1.9}O_{19}$ (Wittmann et al. 1958)

551   and terrestrial Ti^{4+} hibonite (Nagashima et al. 2010). The a and c parameters of $CaAl_{10.1}Ti_{1.9}O_{19}$

552   (Wittmann et al. 1958) are clearly displaced from the trends defined by the other samples (Figure

553   6a, b). If the cell parameters and chemistry of this sample are accurate, then the rate of increase of

554   the unit-cell parameters as a function of Ti pfu is smaller for Ti^{3+} end-member hibonites than for

555   Ti^{4+}-bearing hibonites. Certainly the increase in the unit-cell parameters relative to $CaAl_{12}O_{19}$ of

556   the two Ti^{3+} end-member hibonites of this study is very small. The difference in unit-cell

557   parameters as a function of Ti pfu for the Ti^{3+} end-member and Ti^{4+}-bearing hibonites is not related

558   to the relative sizes of the two Ti cations but is more likely to be associated with the additional

559   complexity of the Ti^{4+} substitution mechanism, which involves both Mg^{2+} and Ti^{4+} and the M2, M3

560   and M4 sites. The unit-cell parameters of the mixed-valent samples are collinear with those of the

561   Ti^{4+} samples both as a function of total Ti pfu (Figure 6) and also as a function of Ti^{4+} pfu (Figure

562   7). This strongly suggests that the driving force for the greater rate of increase of the unit-cell

563   parameters for the Ti^{4+} end-members relative to the Ti^{3+} end-members predominates in the mixed-

564   valent samples.

565

566   With Ti being accommodated only in the R-block layers it may be expected that distortions in

567   this layer will dominate the expansion of the unit cell as a function of increasing Ti (c > a). This,

568   however, is not the case with the expansion parallel to z being dominated by the S-block. Indeed,

569   the expansion of the R-block along z (given by the O1-O1 distance) appears to be negligible across

570   most of the series (Table 7), with a measurable expansion only occurring in the sample with the

571   largest Ti pfu, (1.37, 0.39), where >50% of the M4-M4 pairs are Ti-Ti rather than Al-Al. The c

572   unit-cell edge comprises two R-blocks and two S-blocks and although the S-block is only directly

573   involved in the substitution of Ti into hibonite through occupancy of M3 by Mg^{2+}, this structural

17

574 unit accounts for the entire expansion of the *c* parameter (Figure 6, Table 7) for all samples except

575 (1.37, 0.39). As Mg^{2+} is larger than Al^{3+} (Shannon 1976) the interatomic distances within M3

576 increase linearly as a function of Mg^{2+}, and are inherently a good indicator of the amount of Ti^{4+} in

577 a hibonite structure (Figure 8). The M3-O2 distance, which is parallel to *z,* expands by twice as

578 much as the M3-O4 distance, and the ~ 0.1 Å by which M3-O2 expands across the series accounts

579 for the total expansion of the *c* unit cell edge (~ 0.2 Å), which contains two M3-O2 distances. This

580 suggests that other structural modifications within this unit do not contribute to changes in the unit

581 cell. The $M5O_6$ octahedra connect the M3 sites, into which Mg^{2+} substitutes, and the R-block, into

582 which Ti substitutes. As such $M5O_6$ is sensitive to the effects of both Mg^{2+} and Ti^{4+} substituting

583 into hibonite and the M5-O distances vary linearly towards ~1.9 Å as a function of Ti^{4+} (Figure 9).

584

585   Within the R-block the M2-O1a and M2-O1b distances decrease and increase linearly as a

586 function of Ti pfu respectively (Figure 10a,b). Consequently, the axial off-centring of the M2 cation

587 also increases linearly as a function of Ti. Furthermore, there is a concomitant increase in the

588 equatorial M2-O3 distances (Table 7). As only Ti^{4+} is replacing Al^{3+} on the M2 site, it may be

589 possible to resolve the influence of Ti^{4+} directly upon the observed structural modifications within

590 the $M2O_5$ polyhedra. While the M2-O distances and the axial off-centring of the M2 cation all vary

591 linearly with Ti^{4+} (e.g. Figure 10c) there is no correlation with Ti^{3+}. With both Ti^{3+} and Ti^{4+}

592 substituting onto the M4 sites and Ti-Ti interactions occurring across the shared face of the $M4_2O_9$

593 pairs it is not possible to resolve individual Ti^{3+}- or Ti^{4+}-dependent variations in the interatomic

594 distances within the $M4O_6$ octahedra. However, the M4-M4 distance across the shared face of the

595 $M4_2O_9$ pairs increases linearly as a function of Ti^{4+} pfu (Figure 11a). Constrained by the non-

596 varying thickness of the R-block as a function of Ti, the linear expansion of the M4-O3 distance

597 with Ti is offset by the linear decrease in the M4-O5 distance as a function of Ti^{4+} (Figure 11b,c),

598 aside from sample (1.37, 0.39) where >50% of the M4 sites are Ti rather than Al.

599

600   **Implications**

601   Hibonite has been proposed as a single mineral oxybarometer that can provide an indication

602 of the f_{O2} conditions prevalent at the time of its formation either within the early solar nebula or

603 during some later reprocessing event (Ihinger and Stolper 1986; Beckett et al. 1988). Hibonite

604 oxybarometry has been attempted for CAIs within the Murchison and Allende carbonaceous

605 chondrites. Estimates of f_{O2} determined by optical absorption spectroscopy are up to 10 times more

606 oxidised that those expected in the solar nebula (Ihinger and Stolper 1986), while those from ESR

607 spectroscopy span nine orders of magnitude (Beckett et al. 1988). Both of these approaches are

608 strongly dependent upon a crystal chemical model in which Ti^{3+} occupies the five-coordinate M2

18

609   site. However, the Rietveld and DFT results of the present study show conclusively that Ti^{3+}

610   occupies the octahedral face-sharing M4 site. Furthermore, DFT calculations find that Ti^{3+}-Ti^{3+}

611   interactions between M4 octahedral pairs are favoured with respect to Al^{3+}-Ti^{3+} interactions, while

612   the substitution mechanisms identified by NPD suggest that Ti^{4+}-Ti^{4+} and Ti^{4+}-Ti^{3+} interactions may

613   also occur. Reinterpretation of the optical and ESR spectra in light of these results indicate that the

614   spectral features utilised for hibonite oxybarometry are not associated with occupancy of M2 by

615   Ti^{3+}, but actually arise from Ti-Ti interactions. When interpreting spectroscopic data in terms of

616    $Ti^{3+}/\Sigma Ti$ and f_{O2} the existence of Ti-Ti interactions, which may not be simply related to the amount

617   of Ti^{3+}, need to be considered.

618

619   In this study, hibonite samples with $Ti^{3+}/\Sigma Ti$ ranging from 0.27 to 1.0 were all prepared at the

620   same f_{O2} ($\log f_{O2}$ = -16 at 1400 °C or 6.3 log units below the iron-wüstite f_{O2} buffer). This

621   illustrates how Ti^{4+} can be stabilised in hibonite by Mg^{2+} even under very reducing conditions. That

622   is, crystal chemistry can stabilise oxidation states independently of f_{O2}. The $Ti^{3+}/\Sigma Ti$ ratio of

623   meteoritic hibonite is thus not necessarily related to the f_{O2} of formation and will be strongly

624   influenced by composition. Furthermore, the placement of an upper limit on f_{O2} based solely upon

625   the blue colour of a crystal of hibonite (Ihinger and Stolper 1986) may need to be reconsidered if

626   crystal chemical controls are able to stabilize Ti^{3+} under nominally oxidising conditions.

627

628

Acknowledgements

638

639

640

19

References

641
642 Abrahams, S.C., Marsh, P. and Brandle, C.D. (1987) Laser and phosphor host $La_{1-x}MgAl_{11+x}O_{19}$ (x

643 = 0.050): Crystal structure at 295 K. Journal of Chemical Physics, 86, 4221-4227.

644

645 Aggarwal, R.L., Sanchez, A., Stuppi, M.M., Fahey, R.E., Strauss, A.J., Rapoport, W.R. and

646 Khattak, C.P. (1988) Residual infrared-absorption in as-grown and annealed crystals of Ti-Al_2O_3.

647 IEEE Journal of Quantum Electronics, 24, 1003-1008.

648

649 Allen, J.M., Grossman, L., Davis, A.M. and Hutcheon, I.D. (1978) Mineralogy, textures and mode

650 of formation of a hibonite-bearing Allende inclusion. Proceedings of the 9th Lunar and Planetary

651 Science Conference, 1, 1209-1233.

652

653 Amelin, Y., Krot, A.N., Ulyanov, A.A. and Hutcheon, I.D. (2002) Lead isotopic ages of chondrules

654 and calcium-aluminium-rich inclusions. Science, 297, 1678-1683.

655

656 Armstrong, J.T., Meeker, G.P., Huneke, J.C. and Wasserburg, G.J. (1982) The Blue Angel: I. The

657 mineralogy and petrogenesis of a hibonite inclusion from the Murchison meteorite. Geochimica et

658 Cosmochimica Acta, 46, 575-595.

659

660 Barret, J.P., Gourier, D. and Vivien, D. (1985) Influence of titanium impurities on the chemical

661 alteration of β- and β''-alumina in sodium environment. ESR study. Solid State Ionics, 15, 127-134.

662

663 Beckett, J.R., Live, D., Tsay, F.-D., Grossman, L. and Stolper, E. (1988) Ti^{3+} in meteoritic and

664 synthetic hibonite. Geochimica et Cosmochimica Acta, 52, 1479-1495.

665

666 Bermanec, V.V., Holtstam, D., Sturman, D., Criddle, A.J., Back, M.E. and Scavnicar, S. (1996)

667 Nezilovite, a new member of the magnetoplumbite group, and the crystal chemistry of

668 magnetoplumbite and hibonite. The Canadian Mineralogist, 34, 1287-1297.

669

670 Berry, A.J., Danyushevsky, L.V., O'Neill, H.St.C., Newville, M. and Sutton, S.R. (2008) Oxidation

671 state of iron in komatiitic melt inclusions indicates hot Archaean mantle. Nature, 455, 960-963.

672

673 Berry, A.J., Walker, A.M., Hermann, J., O'Neill, H.St.C., Foran, G.J. and Gale, J.D. (2007)

674 Titanium substitution in forsterite. Chemical Geology, 242, 176-186.

675 doi:10.1016/j.chemgeo.2007.03.010.

20

676

677   Bettman, M. and Peters, C.R. (1969) The crystal structure of $Na_2O.MgO.5Al_2O_3$ with reference to

678    $Na_2O.5Al_2O_3$ and other isotypal compounds. Journal of Physical Chemistry, 73, 1774-1780

679

680   Bischoff, A. and Srinivasan, G. (2003) ^{26}Mg excess in hibonites of the Rumuruti chondrite Hughes

681   030. Meteoritics and Planetary Science, 38, 5-12.

682

683   Burns, R.G. and Burns, V.M. (1984) Crystal chemistry of meteoritic hibonites. Journal of

684   Geophysical Research, 89, 313-321.

685

686   Cramer, C. J. and Truhlar, D. G. (2009) Density functional theory for transition metals and

687   transition metal chemistry. Physical Chemistry Chemical Physics, 11, 10757-10816.

688

689   Curien, H., Guillemin, C., Orcel, J. and Sternberg, M. (1956) La hibonite, nouvelle espèce minérale.

690   Comptes Rendus de l'Académie des Sciences, Paris. 2845-2847.

691

692   Davis, A.M., Tanaka, T., Grossman, L., Lee, T. and Wasserburg, G.J. (1982) Chemical composition

693   of HAL, an isotopically-unusual Allende inclusion. Geochimica et Cosmochimica Acta, 46, 1627-

694   1651.

695

696   De Aza, A.H., Iglesias, J.E., Pena, P. and De Aza, S. (2000) Ternary system Al_2O_3-MgO-CaO: Part

697   II, phase relationships in the subsystem Al_2O_3-$MgAl_2O_4$-$CaAl_4O_7$. Journal of the American Ceramic

698   Society, 83, 919-927.

699

700   Doyle, P.M. (2012) Ti substitution mechanisms in hibonite and the determination of Ti^{3+}/Ti^{4+} by X-

701   ray absorption spectroscopy for use as an oxybarometer with application to early Solar System

702   processes. PhD Thesis, Imperial College London.

703

704   Du, L.L. and Stebbins, J.F. (2004) Calcium and strontium hexaluminates: NMR evidence that

705   "pentacoordinate" cation sites are four-coordinated. The Journal of Physical Chemistry. B,

706   Condensed Matter, Materials, Surfaces, Interfaces & Biophysical, 108, 3681-3685.

707

708   Fuchs, L.H., Olsen, E. and Jensen, K.J. (1973) Mineralogy, mineral-chemistry, and composition of

709   the Murchison (C2) meteorite. Smithsonian Contributions to the Earth Sciences, 10, 1-39.

710

21

711   Graetsch, H.H. and Gebert, W. (1995) Cation distribution in magnetoplumbite type $SrTi_6Co_6O_{19}$.

712   Zeitschrift für Kristallographie, Kristallgeometrie, Kristallphysik, Kristallchemie, 210, 9-13.

713

714   Graetsch, H.H. and Gebert, W. (1996) Short Cr^{3+}-Cr^{3+} distances in magnetoplumbite type

715   $SrCr_9Ga_3O_{19}$. Zeitschrift für Kristallographie, Kristallgeometrie, Kristallphysik, Kristallchemie,

716   211, 25-30.

717

718   Grey, I.E., Madsen, I.C. and Haggerty, S.E. (1987) Structure of a new upper-mantle,

719   magnetoplumbite-type phase, $Ba[Ti_3Cr_4Fe_4Mg]O_{19}$. American Mineralogist, 72, 633-636.

720

721   Grossman, L., Beckett, J.R., Fedkin, A.V., Simon, S.B. and Ciesla, F.J. (2008) Redox conditions in

722   the solar nebula: observational, experimental, and theoretical constraints. Mineralogical Society of

723   America: Reviews in Mineralogy and Geochemistry 68, 93-140.

724

725   Hohenberg, P. and Kohn, W. (1964) Inhomogeneous electron gas. Physical Review, 136, 864–871.

726

727   Hofmeister, A.M., Wopenka, B. and Locock, A.J. (2004) Spectroscopy and structure of hibonite,

728   grossite, and $CaAl_2O_4$: Implications for astronomical environments. Geochimica et Cosmochimica

729   Acta 68, 4485-4503.

730

731   Holtstam, D. (1996) Iron in hibonite: a spectroscopic study. Physics and Chemistry of Minerals, 23,

732   452-460.

733

734   Ibberson, R.M., David, W.I.F. and Knight, K.S. (1992) The high resolution neutron powder

735   diffractometer (HRPD) at ISIS - A user guide. Report RAL-92-031.

736

737   Ihinger, P.D. and Stolper, E. (1986) The color of meteoritic hibonite: an indicator of oxygen

738   fugacity. Earth and Planetary Science Letters, 78, 67-79.

739

740   Ireland, T.R. (1988) Correlated morphological, chemical, and isotopic characteristics of hibonites

741   from the Murchison carbonaceous chondrite. Geochimica et Cosmochimica Acta 52, 2827-2839.

742

743   Iyi, N., Takekawa, S. and Kimura, S. (1989) Crystal chemistry if hexaaluminates: β-alumina and

744   magnetoplumbite structures. Journal of Solid State Chemistry, 83, 8-19.

745

22

746   Junquera, J., Paz, O., Sánchez-Portal, D. and Artacho, E. (2001) Numerical atomic orbitals for

747   linear-scaling calculations. Physical Review B, 64, art. no. 235111.

748   doi:10.1103/PhysRevB.64.235111.

749

750   Kato, K. and Saalfeld, H. (1968) Verfeinerung der Kristallstruktur von $CaO.6Al_2O_3$. Neues

751   Jahrbuch für Mineralogie, Abhandlungen, 109, 192-200.

752

753   Kohn, J.A. and Eckart, D.W. (1964) New hexagonal ferrite, establishing a second structural series.

754   Journal of Applied Physics, 35, 968-969.

755

756   Kohn, W. and Sham, L.J. (1965) Self-consistent equations including exchange and correlation

757   effects. Physical Review, 140, 1133–1138.

758

759   Kreber, E.E. and Gonser, U.U. (1976) Determination of cation distribution in Ti^{4+} and Co^{2+}

760   substituted barium ferrite by Mössbauer spectroscopy. Applied Physics, 10, 175-180.

761

762   Krot, A.N., Fagan, T.J., Keil, K., McKeegan, K.D., Sahijpal, S., Hutcheon, I.D., Petaev, M.I. and

763   Yurimoto, H. (2004) Ca, Al-rich inclusions, amoeboid olivine aggregates, and Al-rich chondrules

764   from the unique carbonaceous chondrite Acfer 094: I. mineralogy and petrology. Geochimica et

765   Cosmochimica Acta, 68, 2167-2184.

766

767   Krot, A., McKeegan, K., Huss, G., Liffman, K., Sahijpal, S. and Hutcheon, I. (2006) Aluminium-

768   magnesium and oxygen isotope study of relict Ca-Al-rich inclusions in chondrules. Astrophysical

769   Journal, 639, 1227-1237

770

771   Larson, A.C. and Von Dreele, R.B. (1994) General Structure Analysis System (GSAS), Los Alamos

772   National Laboratory Report. LAUR 86-748 (revised version).

773

774   Leslie, M. and Gillan, M.J. (1985) The energy and elastic dipole tensor of defects in ionic crystals

775   calculated by the supercell method. Journal of Physics C: Solid State Physics, 18, 973-982.

776

777   Lodders, K. (2003) Solar System abundances and condensation temperatures of the elements.

778   Astrophysical Journal, 591, 1220-1247.

779

780   Nagashima, M., Armbruster, T. and Hainschwang, T. (2010) A temperature-dependent structure

23

781   study of gem-quality hibonite from Myanmar. Mineralogical Magazine, 74, 871-885.

782

783   Paglia, G., Rohl, A.L., Buckley, C.E. and Gale, J.D. (2005) Determination of the structure of γ-

784   alumina from interatomic potential and first-principles calculations: The requirement of significant

785   numbers of nonspinel positions to achieve an accurate structural model. Physical Review B, 71 art.

786   no. 224115. doi:10.1103/PhysRevB.71.224115.

787

788   Palin, E.J., Walker, A.M. and Harrison, R.J. (2008) A computational study of order-disorder

789   phenomena in Mg_2TiO_4 spinel (qandilite). American Mineralogist, 93, 1363-1372.

790   doi:10.2138/am.2008.2896.

791

792   Perdew, J.P., Burke, K. and Emzerhof, M. (1996) Generalized gradient approximation made simple.

793   Physical Review Letters, 77, 3865–3868.

794

795   Rager, H., Geiger, C.A. and Stahl, A. (2003) Ti(III) in synthetic pyrope: A single-crystal electron

796   paramagnetic resonance study. European Journal of Mineralogy, 15, 697-699.

797

798   Rakotondrazafy, M.A.F., Moine, B. and Cuney, M. (1996) Mode of formation of hibonite

799   ($CaAl_{12}O_{19}$) within the U-Th skarns from the granulites of S-E Madagascar. Contributions to

800   Mineralogy and Petrology, 123, 190-201.

801

802   Rietveld, H.M. (1969) A profile refinement method for nuclear and magnetic structures. Journal of

803   Applied Crystallography, 2, 65-71.

804

805   Rietveld, H.M. (2000) The early days: a retrospective view, in Young, R.A. ed., The Rietveld

806   Method: Oxford University Press, 39-42.

807

808   Rout, S.S. and Bischoff, A. (2008) Ca, Al-rich inclusions in Rumurud (R) chondrites. Meteoritics

809   and Planetary Science, 43, 1439-1464.

810

811   Rout, S.S., Bischoff, A., Nagashima, K., Krot, A.N., Huss, G.R. and Keil, K. (2009) Oxygen- and

812   magnesium-isotope compositions of calcium-aluminum-rich inclusions from Rumuruti (R)

813   chondrites. Geochimica et Cosmochimica Acta, 73, 4264-4287.

814

24

815   Sanchez, A., Strauss, A.J., Aggarwal, R.L. and Fahey, R.E. (1988) Crystal-growth, spectroscopy,

816   and laser characteristics of Ti-Al$_2$O$_3$. IEEE Journal of Quantum Electronics, 24, 955-1002.

817

818   Schofield, P.F., Knight, K.S., Covey-Crump, S.J., Cressey, G. and Stretton, I.C. (2002) Accurate

819   quantification of the modal mineralogy of rocks when image analysis is difficult. Mineralogical

820   Magazine, 66, 189–200.

821

822   Schofield, P.F., Smith, A.D., Mosselmans, J.F.W., Ohldag, H., Scholl, A., Raoux, S., Cressey, G.,

823   Cressey, B.A., Quinn, P.D., Kirk, C.A. and Hogg, S.C. (2010) X-ray spectromicroscopy of mineral

824   intergrowths in the Santa Catharina meteorite. Geostandards and Geoanalytical Research, 34, 145-

825   159.

826

827   Sears, V.F. (1992) Neutron scattering lengths and cross sections. Neutron News, 3, 26-37.

828

829   Shannon, R.D. (1976) Revised effective ionic radii and systematic studies of interatomic distances

830   in halides and chalcogenides. Acta Crystallographica, A32, 751-767.

831

832   Simon, S.B., Sutton, S.R. and Grossman, L. (2007) Valence of titanium and vanadium in pyroxene

833   in refractory inclusion interiors and rims. Geochimica et Cosmochimica Acta, 71, 3098-3118.

834

835   Smith, A.D., Schofield, P.F., Cressey, G., Cressey, B.A. and Read, P.D. (2004) The development of

836   X-ray photo-emission electron microscopy (XPEEM) for valence-state imaging of mineral

837   intergrowths. Mineralogical Magazine, 68, 859–869.

838

839   Soler, J.M., Artacho, E., Gale, J.D., García, A., Junquera, J., Ordejón, P. and Sánchez-Portal, D.

840   (2002) The SIESTA method for ab initio order-N materials simulation. Journal of Physics

841   Condensed Matter, 14, 2745–2776.

842

843   Tailby, N.D., Walker, A.M., Berry, A.J., Hermann, J., Evans, K.A., Mavrogenes, J.A., O'Neill,

844   H.St.C., Rodina, I.S., Soldatov, A.V., Rubatto, D. and Sutton, S.R. (2011) Ti site occupancy in

845   zircon. Geochimica et Cosmochimica Acta, 75, 905-921. doi:10.1016/j.gca.2010.11.004.

846

847   Toby, B.H. (2001) EXPGUI, a graphical user interface for GSAS. Journal of Applied

848   Crystallography, 34, 210-221.

849

25

850   Ushikubo, T., Hiyagon, H. and Sugiura, N. (2007) A FUN-like hibonite inclusion with a large

851   ^{26}Mg-excess. Earth and Planetary Science Letters, 254, 115-126.

852

853   Utsunomiya, A.A., Tanaka, K., Morikawa, H., Marumo, F. and Kojima, H. (1988) Structure

854   refinement of CaO.6Al$_2$O$_3$. Journal of Solid State Chemistry, 75, 197-200.

855

856   Vázquez, B.A., Caballero, A. and Pena, P. (2003) Quaternary system Al$_2$O$_3$-MgO-SiO$_2$: I, Study of

857   the crystallization volume of Al$_2$O$_3$. Journal of the American Ceramic Society, 86, 2195-2199.

858

859   Walker, A.M., Hermann, J., Berry, A.J. and O'Neill, H.St.C. (2007) Three water sites in upper

860   mantle olivine and the role of titanium in the water weakening mechanism. Journal of Geophysical

861   Research, 112, art. no. B05211. doi:10.1029/2006JB004620.

862

863   Warren, M.C., Dove, M.T., Myers, E.R., Bosenick, A., Palin, E.J., Sainz-Diaz, C.I., Guiton, B.S.

864   and Redfern, S.A.T. (2001) Monte Carlo methods for the study of cation ordering in minerals.

865   Mineralogical Magazine, 65, 221–248.

866

867   Weber, D. and Bischoff, A. (1994) The occurrence of grossite (CaAl$_4$O$_7$) in chondrites. Geochimica

868   et Cosmochimica Acta, 58, 3855-3877.

869

870   Wittmann, A., Seifert, K. and Nowotny, H. (1958) Ein Beitrag zum Aufbau des Kalzium-Titan(III)-

871   Aluminats. Monatshefte für Chemie, 89, 225-228.

872

873   Woodley, S.M., Gale, J.D., Battle, P.D. and Catlow, C.R.A. (2003) Oxygen ion migration in

874   orthorhombic LaMnO$_{3-\delta}$. Journal of Chemical Physics. 119, 9737-9744.

875

876   Yamaga, M., Yosida, T., Hara, S., Kodama, N. and Henderson, B. (1994) Optical and electron spin

877   resonance spectroscopy of Ti^{3+} and Ti^{4+} in Al$_2$O$_3$. Journal of Applied Physics, 75, 1111-1117.

878

879   Yoneda, S. and Grossman, L. (1995) Condensation of CaO-MgO-Al$_2$O$_3$-SiO$_2$ liquids from cosmic

880   gases. Geochimica et Cosmochimica Acta, 59, 3413-3444.

881

882   Young, R.A. (1993) Introduction to the Rietveld method, in Young, R.A. ed., The Rietveld Method:

883   Oxford University Press, Oxford, pp. 1-38.

884

26

List of Figures

Figure 1. The two structural layers, R-block and S-block, of hibonite with the *c* axis vertical, shown as a composite of both ball-and-stick and polyhedral representations. The R-block comprises the Ca site, the trigonal bipyramidal M2 site and the octahedral face-sharing M4 site. The S-block comprises layers of M5 octahedra interspersed with a layer containing the M3 tetrahedra and the M1 octahedra.

Figure 2. Ti per formula unit (pfu) against Mg pfu for the synthetic samples of this study and meteoritic hibonite. The meteoritic data are from Fuchs et al. (1973), Allen et al. (1978), Armstrong et al. (1982), Davis et al. (1982), Burns and Burns (1984), Ireland (1988), Weber and Bischoff (1994), Bischoff and Srinivasan (2003), Krot et al. (2004), Krot et al. (2006), Ushikubo et al. (2007), Rout et al. (2009), and Doyle (2012).

Figure 3. Observed, calculated and difference profiles for (a) the Ti^{3+} end-member hibonite (0.20,1.0) and (b) the Ti^{4+} end-member hibonite (0.98,0). The dots represent the observed data and the solid lines the calculated profiles.

Figure 4. Ti and Mg pfu of the synthetic hibonite samples determined from Rietveld refinement and energy dispersive spectrometry (EDS).

Figure 5. The occupancy of Ti^{4+} as a fraction of 1 on (a) M2 and (b) M4 as a function of Ti^{4+} pfu.

Figure 6. Unit-cell parameters of Ti-bearing hibonite samples as a function of Ti pfu derived from the Rietveld refinements (solid symbols). (a) *a* cell parameter, (b) *c* cell parameter and (c) *c/a* ratio. The values for $CaAl_{12}O_{19}$, terrestrial Ti^{4+} hibonite (open circle) and synthetic $CaAl_{10.1}Ti_{1.9}O_{19}$ (open square) are taken from Hofmeister et al. (2004), Nagashima et al. (2010) and Wittmann et al. (1958) respectively. For Figures 6-11, where error bars are not visible then symbols are larger than the errors.

Figure 7. Unit-cell parameters of Ti-bearing hibonite samples as a function of Ti^{4+} pfu. (a) *a* cell parameter and (b) *c* cell parameter.

Figure 8. The (a) M3-O2 and (b) M3-O4 distances as a function of Ti^{4+} pfu.

Figure 9. The (a) M5-O1, (b) M5-O2, (c) M5-O4 and (d) M5-O5 distances as a function of Ti^{4+}

27

920   pfu.

921

922   **Figure 10.** The axial (a) M2-O1a and (b) M2-O1b distances as a function of Ti pfu and (c) the M2-

923   O1a distance as a function of Ti^{4+} pfu.

924

925   **Figure 11.** The (a) M4-M4, (b) M4-O3 and (c) M4-O5 distances as a function of Ti pfu.

926

927   **Table 1** Substitution sites of selected cations in natural and synthetic hibonite and various structural

928   analogues.

Site	Hibonite [1,2,3,4,5]	Magnetoplumbite [3,6]	β, β" alumina [7,8]	Sr $Y_{12}O_{19}$ [9,10]	Ba $Y_{12}O_{19}$ [11]
M1	Cr^{3+}	Al^{3+} Cr^{3+}	Al^{3+} Ti^{3+}	Cr^{3+} Ti^{4+}	Fe^{3+} Ti^{4+}
M2	Fe^{2+} Fe^{3+} V^{3+} Ti^{3+} Ti^{4+}	Mn^{4+} Fe^{3+}	Al^{3+}	Co^{2+} Ti^{4+} Ga^{3+}	Fe^{3+} Co^{2+} Ti^{4+}
M3	Mg^{2+} Fe^{2+} Fe^{3+} Zn^{2+} Si^{4+}	Mn^{2+} Zn^{2+} Fe^{3+} Fe^{2+} Mg^{2+}	Al^{3+} Mg^{2+}	Co^{2+} Ga^{3+}	Fe^{3+} Co^{2+}
M4	Fe^{2+} Cr^{3+} Ti^{4+} Si^{4+}	Fe^{3+} Mn^{4+} Sb^{5+} Ti^{4+}	Al^{3+}	Cr^{3+} Ti^{4+}	Fe^{3+} Ti^{4+}
M5	Cr^{3+}	Al^{3+} Mn^{3+} Cr^{3+} Fe^{3+} Ti^{4+}	Al^{3+} Ti^{3+}	Cr^{3+} Ti^{4+} Co^{2+}	Fe^{3+} Co^{2+} Ti^{4+}

929   References: (1) Burns and Burns (1984); (2) Beckett et al. (1988); (3) Bermanec et al. (1996); (4) Holtstam (1996); (5)
930   Nagashima et al. (2010); (6) Grey et al. (1987); (7) Bettman and Peters (1969); (8) Barret et al. (1985); (9) Graetsch and
931   Gebert (1995); (10) Graetsch and Gebert (1996); (11) Kreber and Gonser (1976)

29

932 **Table 2** Chemical composition of synthetic hibonite samples determined by energy dispersive X-ray spectrometry (EDS). The sample nomenclature is of the form

933 (Ti pfu, $Ti^{3+}/\Sigma Ti$). Secondary phases are those identified by NPD and are less than 3 wt%. Standard deviations are in parentheses.

934

Sample	No. analyses	CaO	Al_2O_3	MgO	TiO_2*	Total	Stoichiometry	Secondary phases
(0.20,1.0)	37	8.8 (0.4)	88.2 (0.6)	-	2.4 (0.5)	99.4 (0.7)	$Ca_{1.07}Al_{11.69}Ti_{0.20}O_{19}$	Al_2O_3
(0.33,1.0)	30	8.8 (0.3)	86.7 (0.6)	-	4.0 (0.4)	99.5 (0.8)	$Ca_{1.07}Al_{11.51}Ti_{0.33}O_{19}$	Al_2O_3
(0.62,0.60)	27	8.7 (0.3)	82.8 (0.5)	1.5 (0.1)	7.3 (0.5)	100.2 (0.7)	$Ca_{1.05}Al_{10.99}Ti_{0.62}Mg_{0.24}O_{19}$	-
(0.73,0.33)	42	8.8 (0.3)	79.9 (1.0)	2.9 (0.2)	8.6 (0.7)	100.2 (0.9)	$Ca_{1.07}Al_{10.66}Ti_{0.73}Mg_{0.49}O_{19}$	Al_2O_3
(0.82,0.27)	41	8.6 (0.3)	78.6 (2.5)	3.5 (0.6)	9.6 (2.2)	100.3 (0.9)	$Ca_{1.05}Al_{10.48}Ti_{0.82}Mg_{0.60}O_{19}$	$MgAl_2O_3$
(1.37,0.39)	18	8.6 (0.3)	71.0 (1.1)	4.9 (0.2)	15.9 (0.9)	100.4 (0.8)	$Ca_{1.05}Al_{9.59}Ti_{1.37}Mg_{0.83}O_{19}$	$MgAl_2O_3$, Ti_2O_3
(0.44,0)	26	8.5 (0.3)	83.0 (1.9)	2.5 (0.6)	5.2 (1.4)	99.2 (0.6)	$Ca_{1.04}Al_{11.10}Ti_{0.44}Mg_{0.43}O_{19}$	$MgAl_2O_3$
(0.98,0)	28	8.3 (0.4)	74.8 (0.7)	5.4 (0.2)	11.4 (0.7)	100.0 (0.9)	$Ca_{1.01}Al_{10.07}Ti_{0.98}Mg_{0.91}O_{19}$	$MgAl_2O_3$, $CaTiO_3$

935 * Ti as TiO_2

936

937

938

939

940

941

942

943

944

945

946

947

30

948

949 **Table 3** Lattice parameters and Mg and Ti site occupancies (as fractions of 1) derived from the Rietveld refinements. The occupancies of Ti^{3+} and Ti^{4+} on M4

950 were calculated assuming that Ti^{4+} pfu = Mg^{2+} pfu, Ti^{3+} only occupies M4 and all the Ti on M2 is Ti^{4+}.

951

Sample	a (Å)	c (Å)	Volume (Å^3)	Mg on M3	Ti on M2*	Ti on M4	Ti^{3+} on M4	Ti^{4+} on M4	Ti^{4+} M2/M4 [†]
(0.20,1.0)	5.567260 (6)	21.92612 (4)	588.539 (1)	-	-	0.096 (1)	0.096 (1)	-	-
(0.33,1.0)	5.570159 (9)	21.93871 (6)	589.491 (2)	-	-	0.144 (1)	0.144 (1)	-	-
(0.62,0.60)	5.586154 (7)	21.98939 (5)	594.251 (1)	0.12 (1)	0.020 (5)	0.250 (5)	0.15 (1)	0.10 (1)	0.20 (1)
(0.73,0.33)	5.596009 (8)	22.01478 (5)	597.038 (1)	0.26 (1)	0.040 (5)	0.310 (5)	0.09 (1)	0.22 (1)	0.18 (1)
(0.82,0.27)	5.603373 (9)	22.03238 (6)	599.089 (2)	0.33 (1)	0.065 (3)	0.360 (5)	0.09 (1)	0.27 (1)	0.24 (1)
(1.37,0.39)	5.62894 (1)	22.12121 (7)	607.006 (2)	0.42 (1)	0.050 (5)	0.600 (5)	0.23 (1)	0.37 (1)	0.14 (1)
(0.44,0)	5.58641 (1)	21.99031 (8)	594.329 (4)	0.21 (1)	0.030 (5)	0.190 (5)	-	0.190 (5)	0.16 (1)
(0.98,0)	5.607263 (7)	22.07468 (5)	601.072 (1)	0.46 (1)	0.065 (3)	0.403 (3)	-	0.403 (5)	0.16 (1)

952 * Site is half occupied.

953 † For the hibonite structure M2/M4 calculated in terms of occupancy is equivalent to M2/M4 pfu.

954

955

31

956 **Table 4** Atomic coordinates and isotropic displacement parameters ($U_{iso} \times 100$).

957

		(0.20,1.0)	(0.33,1.0)	(0.62,0.60)	(0.73,0.33)	(0.82,0.27)	(1.37,0.39)	(0.44,0)	(0.98,0)
Ca	x	0.6667	0.6667	0.6667	0.6667	0.6667	0.6667	0.6667	0.6667
	y	0.3333	0.3333	0.3333	0.3333	0.3333	0.3333	0.3333	0.3333
	z	0.2500	0.2500	0.2500	0.2500	0.2500	0.2500	0.2500	0.2500
	U_{iso}	1.14(3)	0.99(5)	2.09(3)	2.03(3)	2.04(4)	3.03(1)	3.15(1)	2.77(4)
M1	x	0	0	0	0	0	0	0	0
	y	0	0	0	0	0	0	0	0
	z	0	0	0	0	0	0	0	0
	U_{iso}	0.73(3)	1.11(5)	0.89(3)	0.82(3)	0.76(4)	0.71(1)	1.06(1)	0.88(4)
M2	x	0	0	0	0	0	0	0	0
	y	0	0	0	0	0	0	0	0
	z	0.2591(1)	0.2598(2)	0.2621(1)	0.2620(1)	0.2620(2)	0.2657(1)	0.2612(1)	0.2641(1)
	U_{iso}	1.71(5)	1.84(8)	2.02(6)	1.92(7)	2.03(9)	1.75(1)	2.02(1)	1.90(4)
M3	x	0.3333	0.3333	0.3333	0.3333	0.3333	0.3333	0.3333	0.3333
	y	0.6667	0.6667	0.6667	0.6667	0.6667	0.6667	0.6667	0.6667
	z	0.02781(5)	0.02878(7)	0.02849(4)	0.02821(4)	0.02861(4)	0.02921(1)	0.02701(1)	0.02791(6)
	U_{iso}	1.07(2)	1.37(3)	1.23(2)	1.15(2)	1.09(2)	0.88(1)	1.17(1)	1.32(4)
M4	x	0.3333	0.3333	0.3333	0.3333	0.3333	0.3333	0.3333	0.3333
	y	0.6667	0.6667	0.6667	0.6667	0.6667	0.6667	0.6667	0.6667
	z	0.19044(5)	0.19029(9)	0.18900(8)	0.1879(1)	0.1875(2)	0.18789(9)	0.1901(1)	0.1865(1)
	U_{iso}	0.65(5)	0.80(9)	1.28(5)	1.07(7)	1.2(1)	1.07(1)	1.13(1)	1.23(4)
M5	x	0.16863(7)	0.1693(1)	0.16908(7)	0.16870(7)	0.16902(9)	0.16774(4)	0.16855(3)	0.16872(2)
	y	0.3372(1)	0.3384(2)	0.3380(1)	0.3373(1)	0.3379(2)	0.3354(1)	0.3371(1)	0.33732(4)
	z	-0.10904(2)	-0.10883(2)	-0.10846(2)	-0.10809(2)	-0.10786(2)	-0.10651(1)	-0.10894(1)	-0.10731(6)
	U_{iso}	1.04(1)	1.30(2)	1.38(1)	1.28(1)	1.27(1)	1.21(1)	1.20(1)	1.40(4)
O1	x	0	0	0	0	0	0	0	0
	y	0	0	0	0	0	0	0	0
	z	-0.14940(3)	-0.14985(4)	-0.14960(3)	-0.15003(3)	-0.15054(4)	-0.14927(1)	-0.15001(8)	-0.15037(6)
	U_{iso}	0.72(2)	1.20(3)	1.27(2)	0.76(2)	0.65(3)	0.66(1)	1.54(1)	1.29(4)
O2	x	0.6667	0.6667	0.6667	0.6667	0.6667	0.6667	0.6667	0.6667
	y	0.3333	0.3333	0.3333	0.3333	0.3333	0.3333	0.3333	0.3333
	z	0.05403(3)	0.05280(6)	0.05458(3)	0.05542(3)	0.05593(4)	0.05668(1)	0.05597(1)	0.05753(6)
	U_{iso}	0.88(2)	0.89(2)	1.17(2)	1.25(2)	1.14(2)	1.38(1)	1.18(5)	1.30(4)
O3	x	0.18166(6)	0.1817(1)	0.18033(6)	0.18049(6)	0.18094(7)	0.17842(4)	0.17986(3)	0.18101(2)
	y	0.3634(1)	0.3635(2)	0.3608(1)	0.3611(1)	0.3620(1)	0.3570(1)	0.3598(1)	0.3621(1)
	z	0.2500	0.2500	0.2500	0.2500	0.2500	0.2500	0.2500	0.2500
	U_{iso}	1.24(1)	1.70(2)	1.67(1)	1.65(1)	1.58(2)	1.09(1)	1.48(1)	1.58(4)
O4	x	0.15600(4)	0.15542(6)	0.15465(3)	0.15400(4)	0.15341(4)	0.15303(4)	0.15398(3)	0.15251(2)
	y	0.31200(8)	0.3108(1)	0.30931(7)	0.30801(7)	0.30682(8)	0.30608(8)	0.30797(7)	0.30502(4)
	z	0.05210(1)	0.05261(2)	0.05238(1)	0.05278(1)	0.05300(2)	0.05329(1)	0.05263(1)	0.05332(1)
	U_{iso}	0.97(1)	1.27(1)	1.37(1)	1.34(1)	1.34(1)	0.86(1)	1.24(1)	1.48(4)
O5	x	0.50357(5)	0.50303(8)	0.50412(4)	0.50455(4)	0.50469(5)	0.50609(4)	0.50367(3)	0.50419(2)
	y	1.0072(1)	1.0061(2)	1.00833(8)	1.00918(8)	1.0095(1)	1.01225(8)	1.00743(7)	1.00846(4)
	z	0.14899(1)	0.14887(1)	0.14893(1)	0.14935(1)	0.14934(2)	0.14949(1)	0.14922(1)	0.14978(1)
	U_{iso}	1.00(1)	1.27(1)	1.32(1)	1.35(1)	1.29(1)	0.75(1)	1.13(1)	1.26(4)

958

959

32

960 **Table 5** Energies of isolated defects at 0 K.

961

Defect (Kröger-Vink notation)	Energy (eV / 256 atom cell)	Notes
No defect	-88959.2740	$CaAl_{12}O_{19}$ hibonite, 256 atoms
$Ti_{Al(1)}^{x}$	-90393.3591	Ti^{3+} on M1
$Ti_{Al(2)}^{x}$	-90394.1357	Ti^{3+} on M2
$Ti_{Al(3)}^{x}$	-90393.8763	Ti^{3+} on M3
$Ti_{Al(4)}^{x}$	-90393.8734	Ti^{3+} on M4
$Ti_{Al(5)}^{x}$	-90393.7426	Ti^{3+} on M5
$Ti_{Al(1)}^{\bullet}$	-90387.3766	Ti^{4+} on M1
$Ti_{Al(2)}^{\bullet}$	-90389.3807	Ti^{4+} on M2
$Ti_{Al(3)}^{\bullet}$	-90387.9251	Ti^{4+} on M3
$Ti_{Al(4)}^{\bullet}$	-90389.0742	Ti^{4+} on M4
$Ti_{Al(5)}^{\bullet}$	-90388.5411	Ti^{4+} on M5
$Mg_{Al(1)}^{'}$	-89836.9945	Mg^{2+} on M1
$Mg_{Al(2)}^{'}$	-89836.2080	Mg^{2+} on M2
$Mg_{Al(3)}^{'}$	-89837.8229	Mg^{2+} on M3
$Mg_{Al(4)}^{'}$	-89836.0045	Mg^{2+} on M4
$Mg_{Al(5)}^{'}$	-89836.6277	Mg^{2+} on M5

962

963

964

965

33

966

967   **Table 6** Energies of clustered defect structures including Ti-Mg and Ti-Ti interactions at 0 K. Defects

968   labeled with (a) and (b) subscripts occur as multiple symmetrically distinct clusters, which can be

969   distinguished using the Ti-Mg distances.

Defect (Kröger-Vink notation)	Energy (eV / 256 atom cell)	Ti-Mg distance (Å)	Notes
No defect	-88959.2740	-	$CaAl_{12}O_{19}$ hibonite, 256 atoms
$\{Ti_{Al(1)}^{\bullet} Mg_{Al(3)}'\}$	-91267.2759	3.30	Ti^{4+} and Mg^{2+} on M1 and M3
$\{Ti_{Al(1)}^{\bullet} Mg_{Al(5)}'\}$	-91266.0809	2.19	Ti^{4+} and Mg^{2+} on M1 and M5
$\{Ti_{Al(2)}^{\bullet} Mg_{Al(4)}'\}_{(a)}$	-91267.5971	3.45	Ti^{4+} and Mg^{2+} on M2 and M4
$\{Ti_{Al(2)}^{\bullet} Mg_{Al(4)}'\}_{(b)}$	-91267.6954	3.54	Ti^{4+} and Mg^{2+} on M2 and M4
$\{Ti_{Al(2)}^{\bullet} Mg_{Al(5)}'\}_{(a)}$	-91268.1237	3.40	Ti^{4+} and Mg^{2+} on M2 and M5
$\{Ti_{Al(2)}^{\bullet} Mg_{Al(5)}'\}_{(b)}$	-91268.1161	3.61	Ti^{4+} and Mg^{2+} on M2 and M5
$\{Ti_{Al(3)}^{\bullet} Mg_{Al(1)}'\}$	-91266.9784	3.30	Ti^{4+} and Mg^{2+} on M3 and M1
$\{Ti_{Al(3)}^{\bullet} Mg_{Al(5)}'\}_{(a)}$	-91266.4905	3.44	Ti^{4+} and Mg^{2+} on M3 and M5
$\{Ti_{Al(3)}^{\bullet} Mg_{Al(5)}'\}_{(b)}$	-91267.1033	3.33	Ti^{4+} and Mg^{2+} on M3 and M5
$\{Ti_{Al(4)}^{\bullet} Mg_{Al(5)}'\}$	-91267.8774	3.33	Ti^{4+} and Mg^{2+} on M4 and M5
$\{Ti_{Al(4)}^{\bullet} Mg_{Al(4)}'\}$	-91267.5227	2.60	Ti^{4+} and Mg^{2+} on M4 and M4
$\{Ti_{Al(4)}^{\bullet} Mg_{Al(2)}'\}_{(a)}$	-91267.5280	3.45	Ti^{4+} and Mg^{2+} on M4 and M2
$\{Ti_{Al(4)}^{\bullet} Mg_{Al(2)}'\}_{(b)}$	-91267.5610	3.54	Ti^{4+} and Mg^{2+} on M4 and M2
$\{Ti_{Al(5)}^{\bullet} Mg_{Al(5)}'\}_{(a)}$	-91267.2759	2.77	Ti^{4+} and Mg^{2+} on M5 and M5
$\{Ti_{Al(5)}^{\bullet} Mg_{Al(5)}'\}_{(b)}$	-91267.5073	2.84	Ti^{4+} and Mg^{2+} on M5 and M5
$\{Ti_{Al(5)}^{\bullet} Mg_{Al(4)}'\}$	-91266.9258	3.33	Ti^{4+} and Mg^{2+} on M5 and M4
$\{Ti_{Al(5)}^{\bullet} Mg_{Al(2)}'\}_{(a)}$	-91266.8811	3.40	Ti^{4+} and Mg^{2+} on M5 and M2
$\{Ti_{Al(5)}^{\bullet} Mg_{Al(2)}'\}_{(b)}$	-91266.8884	3.61	Ti^{4+} and Mg^{2+} on M5 and M2
$\{Ti_{Al(5)}^{\bullet} Mg_{Al(1)}'\}$	-91267.5402	2.91	Ti^{4+} and Mg^{2+} on M5 and M1
$\{Ti_{Al(5)}^{\bullet} Mg_{Al(3)}'\}_{(a)}$	-91268.3199	3.43	Ti^{4+} and Mg^{2+} on M5 and M3
$\{Ti_{Al(5)}^{\bullet} Mg_{Al(3)}'\}_{(b)}$	-91268.3299	3.32	Ti^{4+} and Mg^{2+} on M5 and M3
$\{Ti_{Al(2)}^{\bullet} Mg_{Al(3)}'\}_{(a)}$	-91269.1850	5.76	Ti^{4+} and Mg^{2+} on M2 and M3
$\{Ti_{Al(2)}^{\bullet} Mg_{Al(3)}'\}_{(b)}$	-91269.2066	5.97	Ti^{4+} and Mg^{2+} on M2 and M3
$\{Ti_{Al(4)}^{\bullet} Mg_{Al(3)}'\}$	-91268.8648	3.59	Ti^{4+} and Mg^{2+} on M4 and M3
$\{Ti_{Al(4)}^{x} Ti_{Al(4)}^{x}\}$	-91830.7191	-	Ti^{3+} on M4
$\{Ti_{Al(4)}^{\bullet} Ti_{Al(4)}^{\bullet} Mg_{Al(3)}' Mg_{Al(3)}'\}$	-93579.4590	3.51 and 3.53	Ti^{4+} and Mg^{2+} on M4 and M3

970

971

34

972   **Table 7** Selected interatomic distances (Å); R = R-block, S = S-block.

973

	(0.20,1.0)	(0.33,1.0)	(0.62,0.60)	(0.73,0.33)	(0.82,0.27)	(1.37,0.39)	(0.44,0)	(0.98,0)
Ca-O3 (×6)	2.78798(3)	2.78945(5)	2.79681(3)	2.80182(3)	2.80573(3)	2.81742(4)	2.79673(2)	2.80769(1)
Ca-O5 (×6)	2.7160(3)	2.7228(5)	2.7224(3)	2.7161(3)	2.7181(4)	2.7190(6)	2.7197(2)	2.7171(2)
M1-O4 (×6)	1.8889(4)	1.8921(6)	1.8883(3)	1.8916(3)	1.8923(4)	1.9016(6)	1.8866(3)	1.8920(2)
M2-O1$_a$	2.006(3)	1.983(4)	1.941(2)	1.937(3)	1.926(4)	1.881(4)	1.951(1)	1.888(3)
M2-O1$_b$	2.406(3)	2.411(4)	2.474(2)	2.465(3)	2.457(4)	2.575(3)	2.447(3)	2.510(3)
M2-O3 (×3)	1.7636(7)	1.766(1)	1.7655(6)	1.7697(7)	1.7765(9)	1.7744(8)	1.7584(3)	1.7857(2)
M3-O2	1.794(1)	1.790(2)	1.8266(9)	1.8411(9)	1.863(1)	1.8998(8)	1.8247(3)	1.8859(3)
M3-O4 (×3)	1.7912(5)	1.7945(7)	1.8070(4)	1.8205(4)	1.8272(5)	1.8369(8)	1.8247(3)	1.8438(4)
M4-O3 (×3)	1.9605(8)	1.964(2)	1.997(1)	2.016(2)	2.021(3)	2.0416(6)	1.985(1)	2.038(2)
M4-O5 (×3)	1.8766(6)	1.873(1)	1.8730(9)	1.864(1)	1.864(2)	1.8865(6)	1.877(1)	1.8471(2)
M5-O1	1.8509(7)	1.864(1)	1.8689(7)	1.8774(8)	1.890(1)	1.8887(8)	1.8643(3)	1.8939(2)
M5-O2	1.9948(8)	2.005(1)	1.9828(7)	1.9730(8)	1.963(1)	1.9555(8)	1.9747(3)	1.9407(3)
M5-O4 (×2)	2.0044(4)	1.9965(7)	1.9970(5)	1.9854(5)	1.9809(6)	1.9609(8)	1.9959(3)	1.9673(4)
M5-O5 (×2)	1.8075(5)	1.8089(7)	1.8148(4)	1.8261(5)	1.8288(6)	1.8527(8)	1.8165(3)	1.8450(4)
M4-M4	2.612(2)	2.620(4)	2.683(4)	2.734(5)	2.754(8)	2.748(4)	2.635(3)	2.803(3)
O1-O1 (R)	4.412(1)	4.394(2)	4.415(1)	4.402(1)	4.383(2)	4.456(4)	4.398(1)	4.398(3)
O1-O1 (S)	6.551(1)	6.575(2)	6.579(1)	6.606(1)	6.634(2)	6.604(4)	6.598(3)	6.639(3)

974

975

976
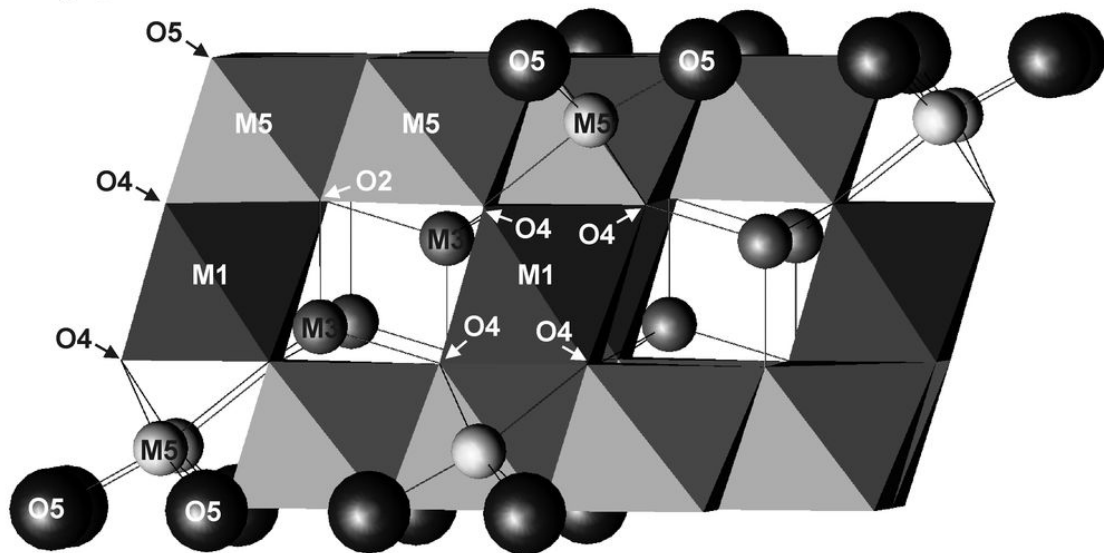
35
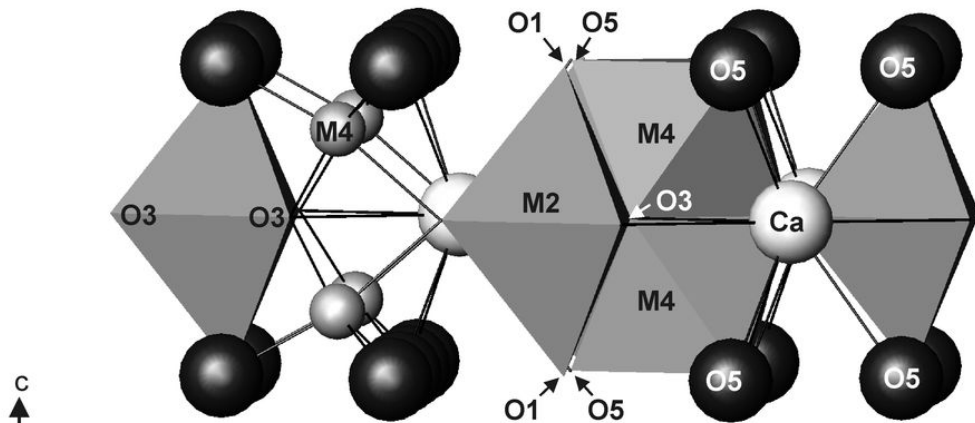
Figure 2   Doyle et al 2013
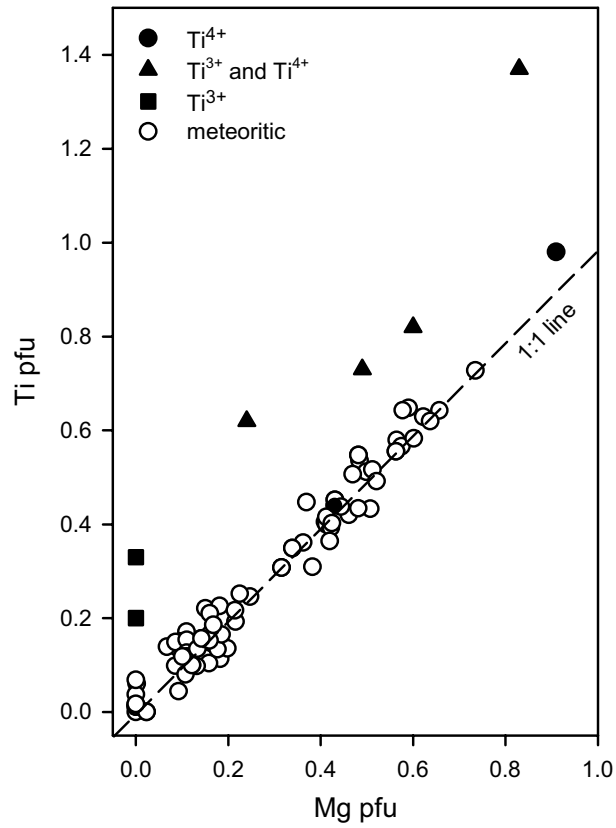
Figure 3   Doyle et al. (2013)
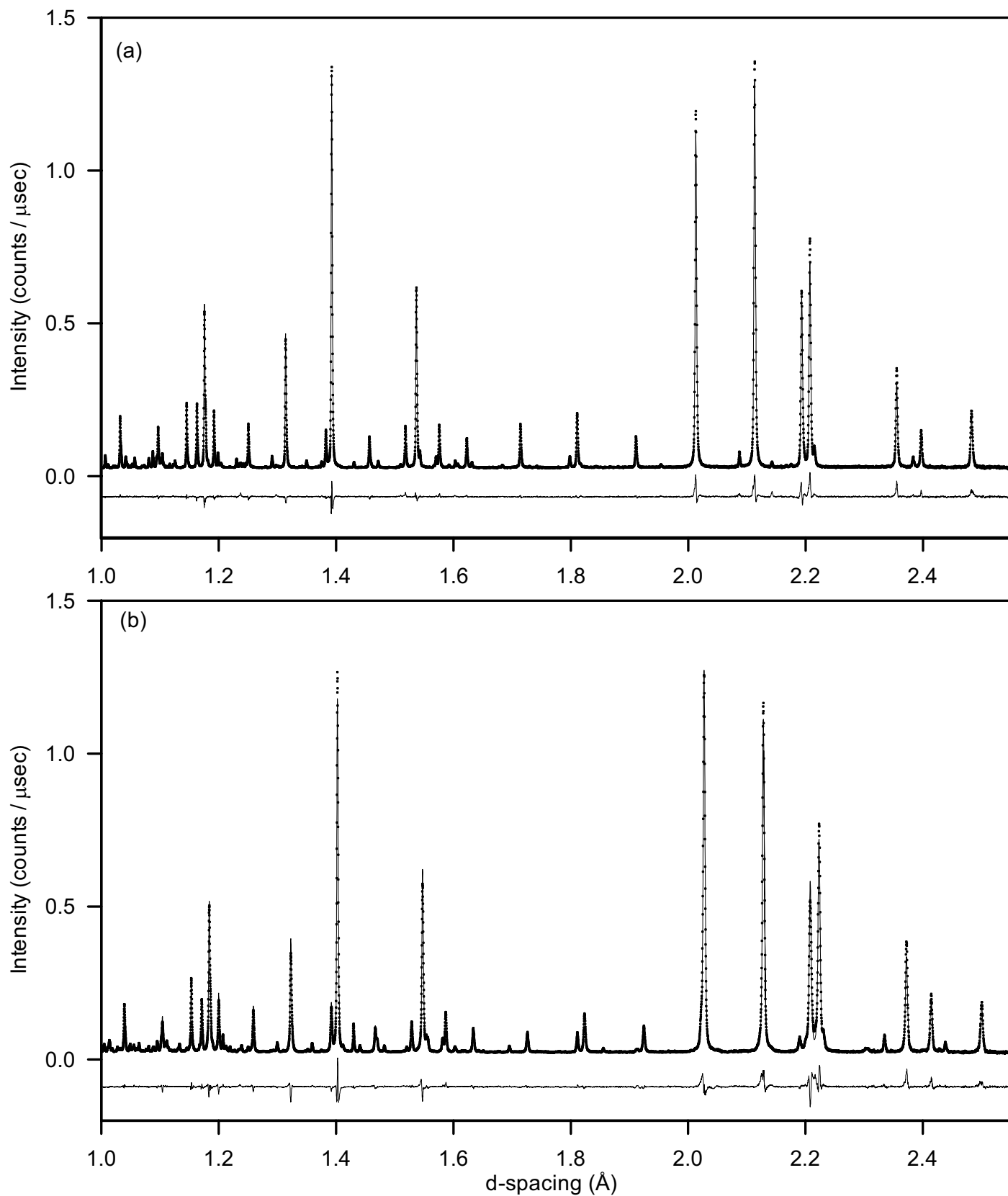
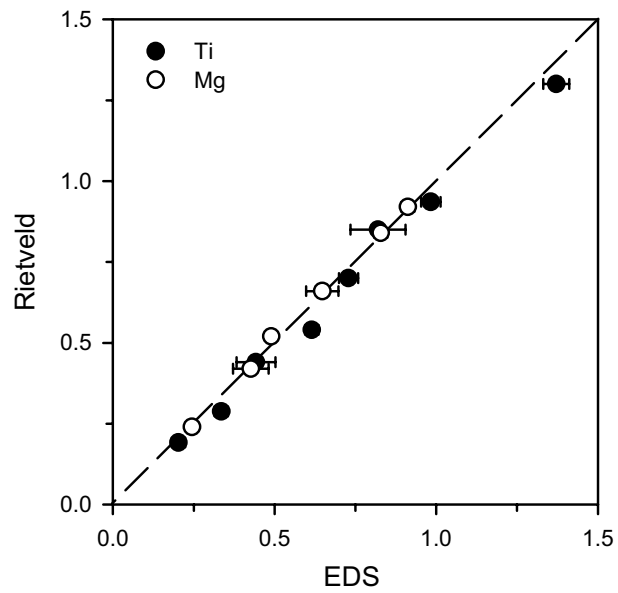Figure 4   Doyle et al. 2013

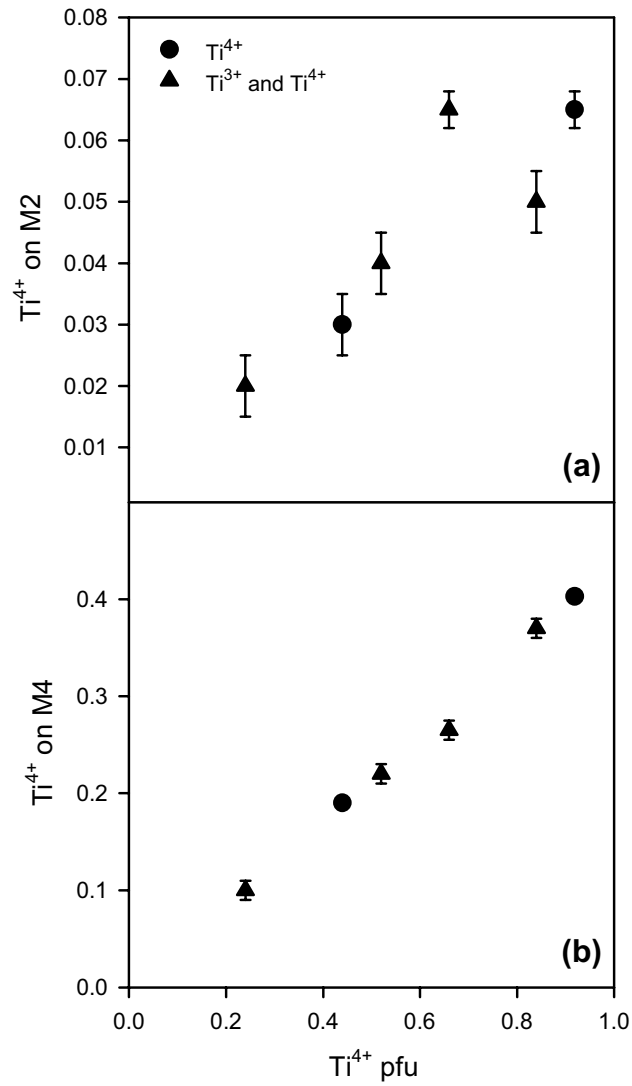Figure 5   Doyle et al. 2013
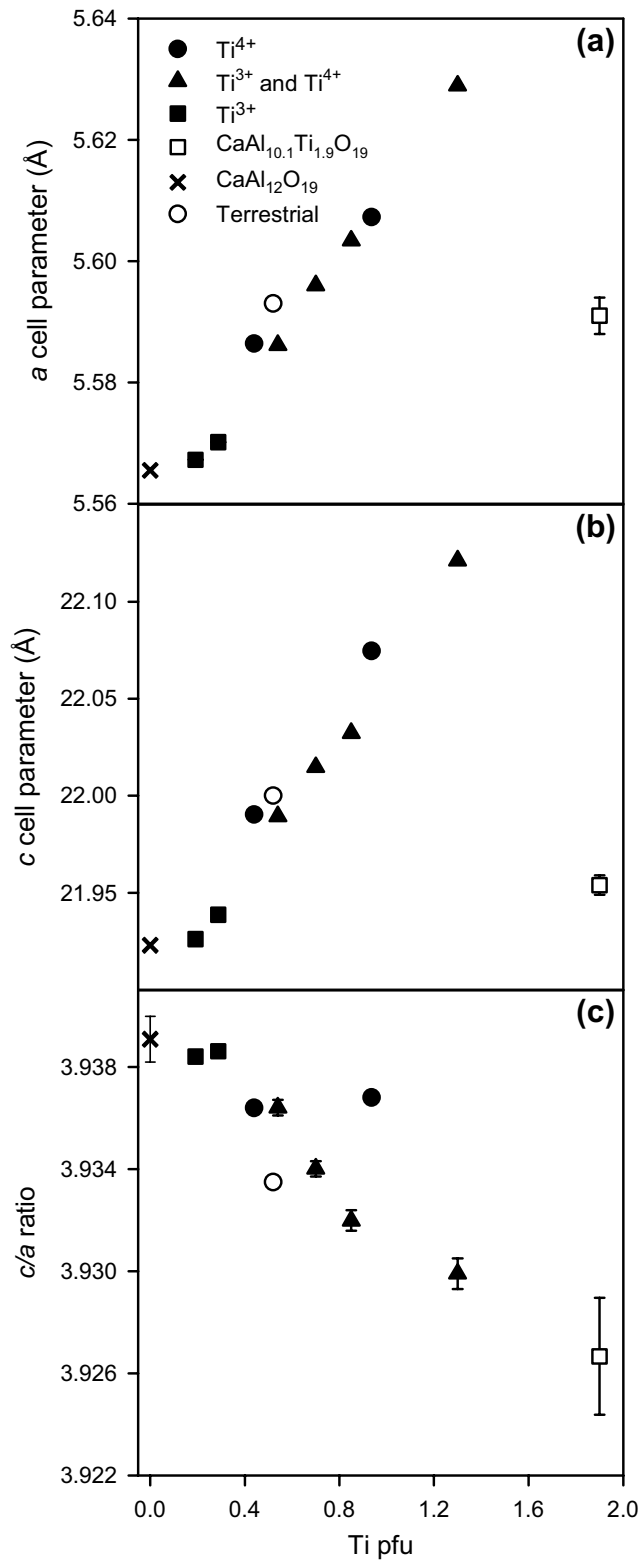
Figure 6   Doyle et al. 2013
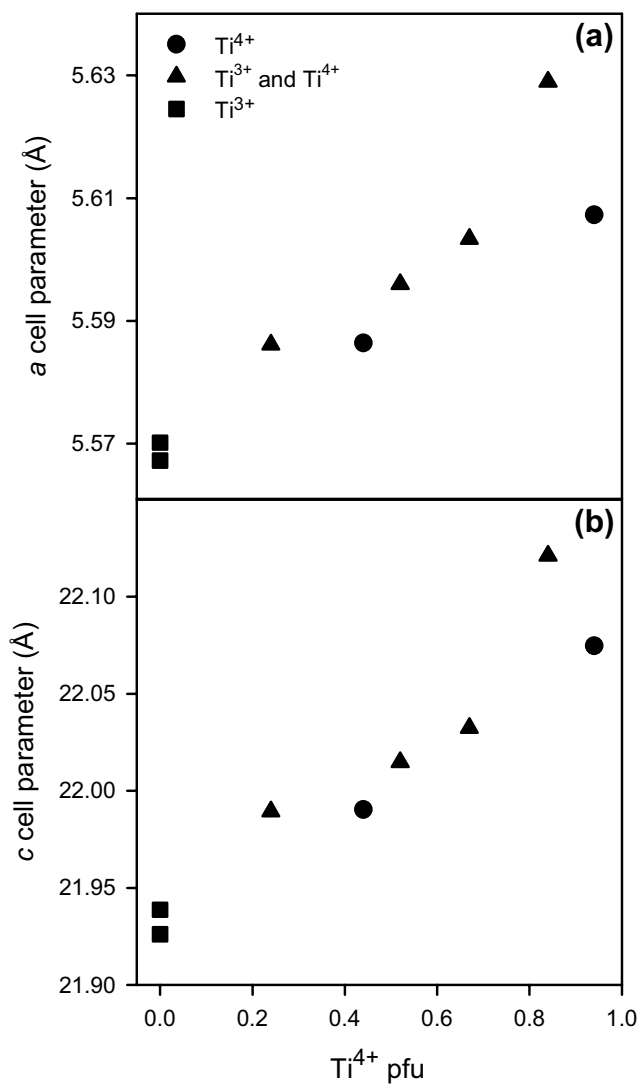
Figure 7   Doyle et al. 2013
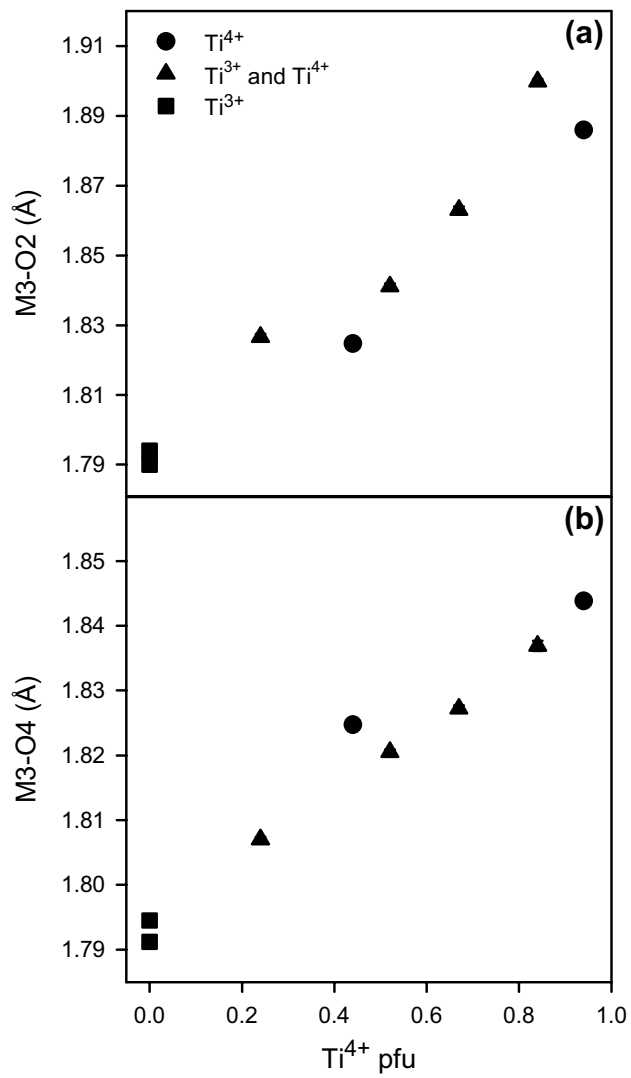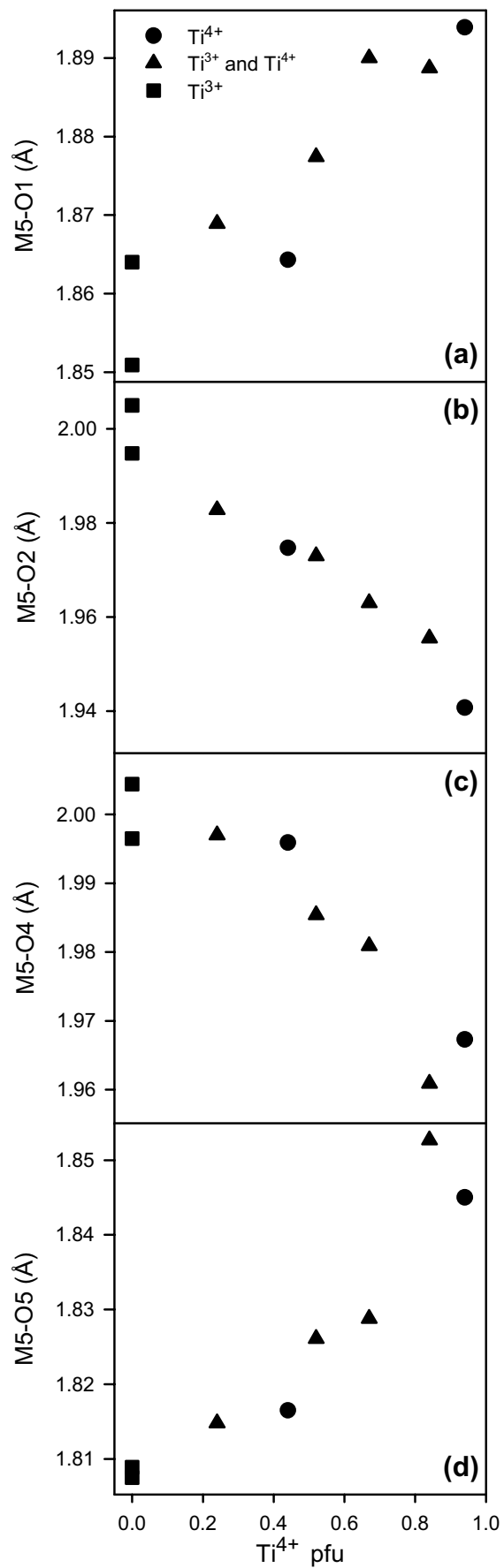
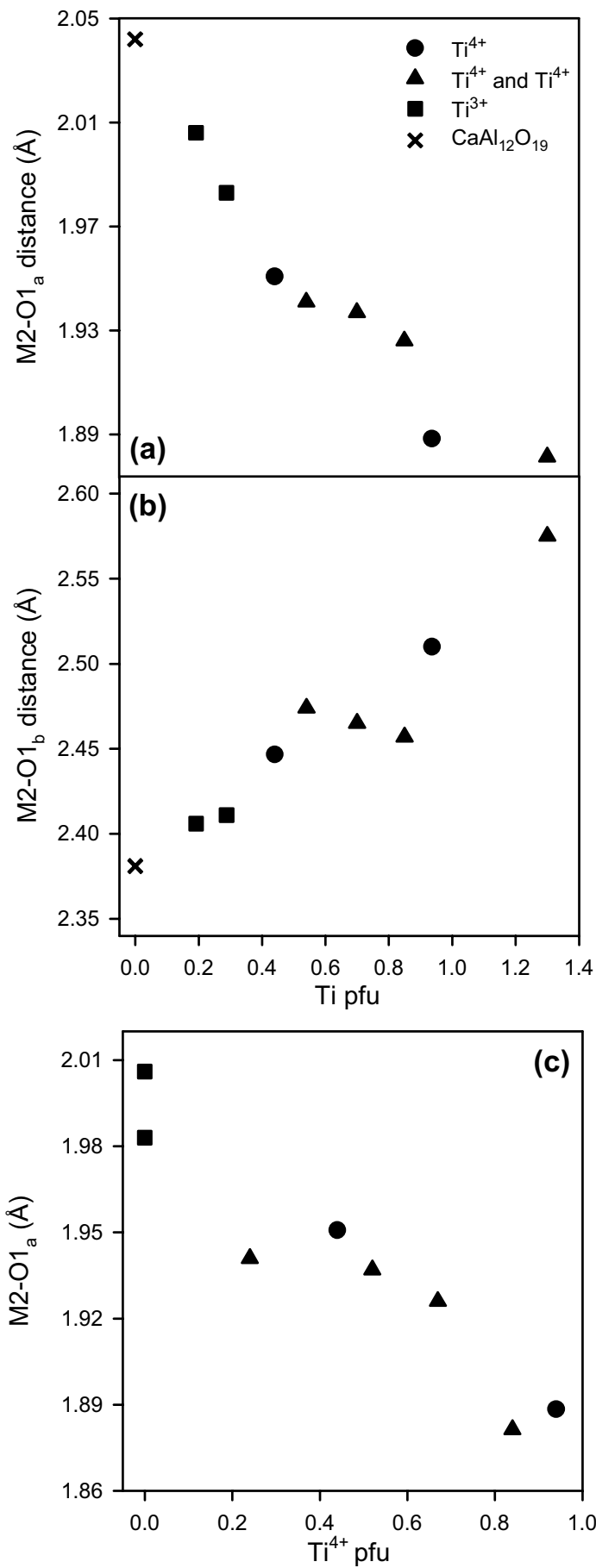Figure 8   Doyle et al. 2013

Figure 9   Doyle et al. 2013

Figure 10   Doyle et al. 2013